

Quantum Algorithm for the Fixed-Radius Neighbor Search

Luca Cappelli

*Dipartimento di Fisica dell'Università di Trieste, via Tiepolo 11, I-34131 Trieste, Italy;
Fondazione Istituto Italiano di Tecnologia, Center for Life Nano-Neuroscience
at la Sapienza, Viale Regina Elena 291, 00161 Roma, Italy
INAF - Osservatorio Astronomico di Trieste, Trieste, Italy;*

Claudio Sanavio*

*Fondazione Istituto Italiano di Tecnologia, Center for Life Nano-Neuroscience
at la Sapienza, Viale Regina Elena 291, 00161 Roma, Italy*

Alessandro Andrea Zecchi†

*MOX – Department of Mathematics
Politecnico di Milano
Piazza L. da Vinci, 32, 20133 Milano, Italy*

Philip Mocz

Center for Computational Astrophysics, Flatiron Institute, 162 5th Ave, New York, NY 10010, USA

Giuseppe Murante

INAF - Osservatorio Astronomico di Trieste, via Tiepolo 11, I-34131 Trieste, Italy;

Sauro Succi

*Fondazione Istituto Italiano di Tecnologia, Center for Life Nano-Neuroscience
at la Sapienza, Viale Regina Elena 291, 00161 Roma, Italy*

(Dated: January 5, 2026)

Neighbor search is a computationally demanding problem, usually both time- and memory-consuming. The main problem of this kind of algorithms is the long execution time due to cache misses. In this work, we propose a quantum algorithm for the Fixed RAdius Neighbor Search problem (FRANS) based on the fixed-point version of Grover's algorithm. We propose an efficient circuit for solving the FRANS with linear query complexity with the number of particles N . The quantum circuit returns the list of all the neighbors' pairs within the fixed radius, together with their distance, avoiding the slow down given by cache miss.

We analyzed the gate and the query complexity of the circuit. Our FRANS algorithm presents a query complexity of $\mathcal{O}(N/\sqrt{M})$, where M is the number of solutions, reaching the optimal lower bound of the Grover's algorithm. We propose different implementations of the oracle, which must be chosen depending on the precise structure of the database. Among these, we present an implementation using the Chebyshev distance with depth $\mathcal{O}(q_1)$, where 2^{q_1} is the number of grid points used to discretize a spatial dimension. State-of-the-art algorithms for state preparation allow for a trade-off between depth and width of the circuit, with a volume (depth \times width) of $\mathcal{O}(N \log(N))$. This unfavorable scaling can be brought down to $\mathcal{O}(\text{poly}(\log N))$ in case of structured datasets. We proposed a stopping criterion based on Bayes interference and tested its validity on 1D simulations. Finally, we accounted for the readout complexity and assessed the resilience of the model to the readout error, suggesting an error correction-free strategy to check the accuracy of the results.

I. INTRODUCTION

With the ceaseless advances of processing speed, scientific computing is entering a regime in which efficient data access policies are becoming prioritary with respect to sheer computing speed [1, 2]. Accessing data can be more costly than processing them, especially in applications based on irregularly distributed or unstructured

data, such as particle methods and Lagrangian formulations of continuum theory, where physical and logical (storage location in memory) distances often diverge. Unstructured data also appear in Eulerian fields in disordered environments, such as flows in porous media [3–5].

A paradigmatic example of this challenge is the Fixed-Radius Neighbor Search (FRANS) [6], which consists in finding all particles within a fixed distance between each other. This Fixed-RAdius Neighbor Search (FRANS) [6] is strictly related to N -body methods and forms the computational backbone of numerous simulation methods across physics, chemistry, and astronomy [7–11], yet consistently dominates runtime despite decades of algo-

* claudio.sanavio@iit.it

† alessandroandrea.zecchi@polimi.it

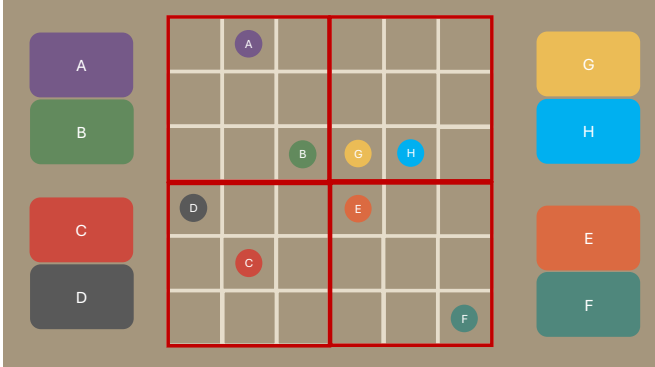


FIG. 1: Toy model illustrating the cache miss problem in neighbor search algorithms. An evenly spaced grid contains eight particles distributed across four memory blocks (indicated by red boundaries). Each particle's data is stored in memory locations denoted by matching colors. Note that spatially adjacent particles might be stored in different memory locations.

rithmic advancements.

The naive approach to finding all particles within a cutoff distance ξ requires examining every possible particle pair, resulting in $\mathcal{O}(N^2)$ scaling that quickly becomes unfavorable as the system size grows. Modern simulations employ specialized spatial data structures such as uniform grids, Verlet lists [7, 10, 12], and hierarchical trees [9, 13], which can reduce the complexity to $\mathcal{O}(N \log N)$ by considering only a portion of all the possible pairs.

Fast algorithms used to explicitly find all the particle pairs within the fixed-radius scale as $\mathcal{O}(M+N)$, where M is the number of neighboring pairs, with a preprocessing of $\mathcal{O}(N \log N)$ and a $\mathcal{O}(N)$ space complexity [14]. Yet, in spite of the improved computational cost, this optimized neighbor search still constitutes the primary computational expense across diverse scientific applications.

In the context of Molecular Dynamics (MD), Verlet lists or cell indices [7] are used to evaluate interactions between atoms for the study of a wide range of phenomena such as drug binding [15, 16], membrane dynamics [17, 18] and material science [19]. These data structures keep track of the atoms that are spatially close, in order to avoid considering atoms far beyond the interaction radius. The FRANS procedure and maintenance of these lists typically consumes from 30% to 60% of total runtime in large-scale simulations [20, 21]. Another interesting field of MD concerns protein folding. Research in this area focuses on how proteins evolve towards an equilibrium state (folding) and interact with one another. A noticeable application is found in neuroscience, where abnormal folding patterns often signal neurological diseases [22]. While earlier studies relied on neighbor search [23], the field has evolved considerably with new approaches. AlphaFold [24] stands out as a particularly valuable tool, serving as a detailed simulator and

providing a database of 200 million proteins' structure. In this case, neighbor search algorithms remain useful for homology detection [25], helping researchers identify structural similarities between proteins to trace evolutionary origins and primitive forms. These methods also assess how well different proteins might interact based on their geometric properties [26]. Non-equilibrium protein folding [27–29] is an open research field, also related to neurological disorder [30, 31] and represents another area of interest for neighbor search. Here environmental influences cause proteins to adopt conformations outside thermal equilibrium. Since ground-state assumptions do not apply in these systems, different methods are used to model the folding mechanism such as coarse-grained molecular dynamics simulations combined with FRANS.

In both cosmology and fluid dynamics, Smoothed Particle Hydrodynamics (SPH) [8] can be used to simulate the evolution of fluids and gases. This approach represents continuous media as discrete particles, each carrying fundamental properties such as mass, momentum and energy. Particle interactions emerge through a weighting scheme that employs localized kernel functions to determine the influence of neighboring particles. The method achieves conservation of field quantities (e.g, pressure and density) by spatially averaging contributions from all particles within the kernel's smoothing length radius. The evaluation of neighboring pair and interaction between particles takes up most of the execution time [32]. The challenge becomes particularly acute in simulations with free surfaces or multiphase flows, where particle distributions become highly non-uniform.

In the context of astrophysical N-Body simulations, SPH is used to simulate dust dynamics using tree-based methods for the neighbor search part. It is common to consider in these scenarios the nearest n neighbors (typically $n = 64$) rather than all particles within a fixed radius [33]. While this can introduce limitations to the convergence of the scheme [34], it remains a practical approach.

For purely gravitational N-body simulations, hybrid Tree-Particle-Mesh methods are often employed to achieve $\mathcal{O}(N \log N)$ scaling, leveraging techniques such as space-filling Peano-Hilbert ordering, Oct-trees, and multi-pole expansions. However, these methods do not explicitly compute interactions for all neighbor pairs within a fixed radius, and thus do not fully fall into the FRANS category. In both cases, the traversal of these spatial data structures to identify nearby particles still dominates computational expense, consuming most of simulation's time in cosmological models with billions of bodies [9, 35]. Highly clustered mass distributions – characteristic of galaxy formation – further amplify these costs by necessitating frequent tree rebuilds.

What makes this problem particularly resistant to optimization is not merely its algorithmic complexity, but rather the challenging computational patterns it creates. Specifically, the combination of a large data structure combined with the frequent and irregular memory access patterns.

To be more specific, modern computing architectures are built around a memory hierarchy (CPU registers \rightarrow L1 cache (32 – 64 KiB per core) \rightarrow L2 cache (512KiB – 8 MiB per core) \rightarrow L3 cache (120 – 256 MiB per core) \rightarrow main memory; data collected from [36, 37]) that performs best when data access follows predictable patterns. However, neighbor search fundamentally involves unpredictable memory access and particles that are close in space configuration might be stored far apart in memory, particularly after many simulation time steps have caused the particles to move from their initial positions. This creates numerous cache misses, as the processor constantly needs to fetch data from slower memory tiers. For reference, in both SPH and MD the number of M depends on the application, as high resolution simulations might require higher values. In the common scenario however, an accurate 3D SPH simulation requires approximately $N = 10^{10}$, with approximately 400 target neighbors per particle [38], while an MD simulation might require $N = 10^8$ with the number of neighbors in the order of hundreds [10, 39, 40].

In Fig. 1 is presented a toy model representing the cache miss problem. When searching for neighbors of particle B, the algorithm needs to access data for particles E, G, and H that happen to be spatially nearby. However, due to limited cache memory capacity, only particles within B’s sub-quadrant are currently stored in cache. To retrieve information for the remaining particles, the algorithm must fetch data from main memory—a significantly slower operation. The frequent repetition of this process creates substantial computational overhead and dramatically increases execution time. Thus, the mismatch between physical proximity and memory proximity causes the FRANS to be the bottleneck in many different scenarios. We note that the toy model in Fig. 1 represents the cache-miss problem in its simplest form. In practice, sophisticated techniques exist to reduce the mismatch between physical and memory proximity, such as ordering particles along Peano-Hilbert space-filling curves [33, 41].

An alternative approach to solving the bottleneck problem can be offered by the framework of quantum computation [42] which in the last two decades has seen a surge of theoretical advances and potential applications [43] in quantum chemistry [44], material science [45], cosmology [46] and computational fluid dynamics [47].

At the dawn of quantum computing, Grover’s search algorithm [48] showed one of the first example of a quantum algorithm that can run faster than any classical algorithm designed for the same task. While the computational complexity of a classical search is $\mathcal{O}(N)$, Grover’s algorithm can do the search with only $\mathcal{O}(\sqrt{N})$ steps, thus offering a quadratic advantage. After its appearance in the literature, Grover’s algorithm has been analyzed and modified several times to match more specific tasks and to tackle the inherited issues of the original algorithm. Among those, we mention the Fixed-point

search (FPS) algorithms [49–51], thought to tackle the periodic increase and decrease in the success probability of the search, and the oblivious amplitude amplification algorithms(OAA) [52–54] intended to overcome the issue of not knowing the target state in advance. We will discuss both approaches later in the main text. In more recent years, it has been shown how Grover’s search algorithm and all of its many versions belong to the class of Quantum Singular-value Transform (QSVT) algorithms [55, 56], which reveals the principles behind the most widely used (and cited) quantum algorithms.

In this work, we aim to find a solution to the FRANS problem by employing our own version of the oblivious-fixed-point amplification algorithm [50, 53], which is very adaptable to different initial states while being agnostic to the target state. The manuscript is structured as follows. In Section II we introduce the problem and describe its difficulties when treated by a classical computer. In Section III we describe the Grover’s algorithm and its FPS and OAA versions. In Section IV we describe our quantum FRANS algorithm and we highlight the similarities and differences with the previous algorithms. Hence, we explicitly show the quantum circuit and the gate decomposition of the various operations, analyzing the computational complexity and the gate complexity. Furthermore, we propose a stopping criterion based on Bayesian’s posterior probability. In Section V we perform numerical test to verify the goodness of our stopping criterion. In Section VI we introduce the bit-flip and the readout measurement errors in our simulation, calculating the threshold for the amount of noise required to preserve the quantum advantage of the algorithm, without introducing particular error correction schemes. Finally, we draw the outlooks and the conclusions of our work in Section VII.

II. THE FIXED-RADIUS NEIGHBOR SEARCH

At the heart of many computational models in physics lies a conceptually simple yet computationally intensive operation: determining which objects in space are close to one another. This procedure, known as neighbor search, forms the foundation for virtually all particle-based simulation methods across the physical sciences.

In its most fundamental form, the fixed-radius variant, neighbor search answers a straightforward question: given a collection of particles distributed throughout space, which particles lie within a fixed distance of each other? This critical calculation enables the modeling of interactions that occur only between objects in close proximity—forces that diminish rapidly with distance, collisions between bodies, or influence that spreads within a limited radius.

The mathematical formulation is deceptively simple. For each particle i in a system of N particles, we must identify all other particles j such that the distance between them $d(r_i, r_j)$ is less than some threshold distance

ξ . This distance threshold might represent the cutoff radius of a potential energy function in MD, the smoothing length in fluid simulations.

Despite its conceptual simplicity, this operation presents an extraordinary computational challenge. The most direct approach—checking every possible pair of particles—would require examining N^2 distance calculations, a prohibitive scaling for systems of scientific interest that may contain millions or billions of particles. Moreover, as particles move throughout a simulation, these neighborhood relationships continually change, requiring repeated recalculation.

To address this challenge, researchers have developed sophisticated spatial data structures that organize particles based on their positions in space. Cell lists divide the simulation domain into a grid, allowing the search to focus only on particles in adjacent cells. Verlet lists maintain a precomputed set of neighbors for each particle, including a buffer zone to reduce update frequency. Tree-based methods hierarchically partition space, enabling rapid elimination of distant regions from consideration.

These techniques reduce the theoretical complexity from $O(N^2)$ to $O(N \log N)$, representing an enormous computational saving. Nevertheless, neighbor search still typically accounts for 30–70% of total computation time in production simulations across disciplines [20, 21, 32]. The persistent challenge stems from a fundamental disconnect between two different types of proximity: spatial proximity in the physical simulation and memory proximity in the computing hardware.

When particles are close to each other in the simulation space, their data should ideally be close to each other in the computer’s memory for efficient processing. However, this alignment rarely occurs, especially as particles move throughout the simulation. A particle’s neighbors in physical space are often scattered across distant memory locations, forcing the processor to constantly fetch data from widely separated memory addresses.

Compounding this problem is the repetitive nature of the search operation. For each of the N particles in the system, the algorithm must perform a separate neighbor search, repeatedly accessing memory locations across the entire data structure.

The combined effect of these two factors – spatial memory misalignment and repeated broad memory access – frequently results in cache misses, where the processor must wait to retrieve data from slower memory tiers rather than finding it in fast cache memory. These waiting periods significantly increase actual execution time, often by an order of magnitude or more compared to theoretical predictions.

Thus, the primary challenge in modern neighbor search implementations has shifted from algorithmic complexity to hardware efficiency. Even algorithms with optimal theoretical scaling ($O(N)$) can perform poorly in practice due to their incompatibility with contemporary computing architectures and the true complexity now lies not in the mathematical operation count but in navigating

the complex memory hierarchy of modern processors to minimize data movement costs.

Estimating the impact of cache misses on the FRANS solution is a complex issue that falls beyond the scope of this work. Such an assessment depends not only on the algorithmic implementation but also on the underlying hardware architecture and specific software realization. Additionally, factors such as dataset size, memory management strategies, and data distribution across computing resources vary significantly between different versions and implementations. Nevertheless, to provide context on how this issue impacts modern simulations, we present a simplified estimate.

Consider a cosmological simulation with 10^{10} particles executed on Fugaku supercomputer [36]. It has been reported that in a 32^3 particles SPH simulation optimized for single-node execution on Fugaku exhibits cache miss probabilities for $L1 = 1.2\%$ and for $L2 = 0.12\%$ [57]. Building on these data, we aim to estimate cache behavior for a 10^{10} -particle simulation under a simplified capacity-dominated scaling model, where the miss rate scales proportionally with the number of particles per node.

Fugaku comprises 158,976 compute nodes [36]. A reasonable allocation for a simulation of this magnitude would utilize approximately one-tenth of the available nodes ($\sim 15,898$ nodes) [58], with each node processing $\sim 6.29 \times 10^5$ particles. Applying a naive linear scaling law, the estimated miss rates increase to $L1 \simeq 23\%$ and $L2 \simeq 2.4\%$.

These estimates provide a first-order approximation of cache behavior, assuming that the per-particle data dimension remains independent of the working set size. However, for larger datasets, a significantly greater fraction of particles resides in RAM compared to the 32^3 particles-per-node case, thereby increasing the probability of accessing particles stored in main memory rather than cache. This type of miss is particularly costly, as retrieving data from main memory requires substantially more CPU cycles than cache access. During such memory fetches, the entire computational pipeline stalls while awaiting the memory refill operation.

Given these considerations, we regard our estimate as an upper bound on the actual cache miss percentage. We emphasize that actual performance may differ substantially depending on code-specific factors, particularly the strategies employed for managing and accessing larger datasets in practice. For instance, codes written for molecular dynamics do not translate well to the astrophysical domain due to fundamentally different data layouts: Verlet lists are optimized for short-range interactions, whereas in cosmological simulations data are clustered in distinct spatial regions separated by cosmic voids. Moreover, state-of-the-art codes employ sophisticated techniques such as Peano-Hilbert space-filling curves [41, 49] to ensure that spatially proximate data occupy adjacent memory locations, thereby minimizing

cache misses. However, the focus of this work is not to compete with these highly optimized classical methods. Rather, we aim to introduce the fundamental elements of a quantum algorithm for the FRANS problem.

III. QUANTUM SEARCH ALGORITHMS

In this section, we describe a few versions of the Grover's algorithm as they are relevant to this paper. In the original work, the N elements of a database D are encoded into a quantum state $|i\rangle$ and we want to select a specific target state $|\psi_T\rangle$. The initial state is set as the uniform superposition of all possible states

$$|\psi_0\rangle = \frac{1}{\sqrt{N}} \sum_{i \in D} |i\rangle. \quad (1)$$

The algorithm consists in applying to the state $|\psi_0\rangle$ first an oracle operator \hat{O} , which is capable of recognizing the solution and whose action is to flip the sign of the target state $|\psi_T\rangle$, defined as

$$\hat{O} = \mathbb{I} - 2|\psi_T\rangle\langle\psi_T|, \quad (2)$$

and later applying the reflection operator \hat{R}_0 , which reflects the resulting state with respect to the initial state $|\psi_0\rangle$, namely

$$\hat{R}_0 = 2|\psi_0\rangle\langle\psi_0| - \mathbb{I}. \quad (3)$$

Conveniently, the algorithm can be represented in a two-dimensional space spanned by the solution $|\psi_T\rangle$ and its orthogonal part $|\psi^\perp\rangle$ in the initial state, defined such that

$$|\psi_0\rangle = \cos\theta|\psi^\perp\rangle + \sin\theta|\psi_T\rangle, \quad (4)$$

where the angle $\theta = \arcsin\left[\sqrt{M/N}\right]$ and M is the number of target states in the database. The application of the Grover operator $\hat{G} = \hat{R}_0\hat{O}$ rotates the vector in the $|\psi_T\rangle, |\psi^\perp\rangle$ plane by an angle 2θ increasing the amplitude of the target state. By applying G a sufficiently large number of times $k \sim \sqrt{N/M}$, the final state $G^k|\psi_0\rangle$ will have the maximum amplitude for the component $|\psi_T\rangle$.

Now we see that there are two main hurdles when one aims to apply the Grover's search algorithm to its database. First, if the value M is unknown, the risk is to apply G too many times, with the result that the final state passes over the $|\psi_T\rangle$ axis and the amplitude probability of measuring the target state reduces. This is known as the *soufflé problem*, since applying the Grover's operator too few times undercooks the state, whereas applying it too many times overcooks it, with the resulting

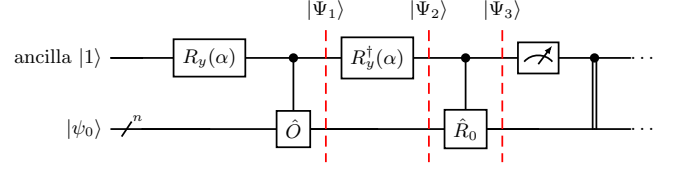


FIG. 2: Circuit used for the amplitude amplification process. Based on Mizel search algorithm. The parameter α is adjusted accordingly to the iteration. The measurement on the ancilla qubit serves as control: if $|0\rangle$ is the outcome, it means that the quantum register is ready for measurement; otherwise repeat the process, varying the angle α .

deflation of the quantum cake. This obstacle was overcome by the FPS algorithm [50], which increases monotonically the probability of measuring a target state. Second, as expressed in Eq. (2), the target state has to be known in order to construct the correct oracle operator \hat{O} . Although this may be sensible in the context of quantum simulation to construct a particular quantum state, it loses its significance when the quantum algorithm is intended to search over a classical database or to solve classical optimization problems. The OAA algorithm was designed to overcome this problem. In the remainder of this section we are going to summarize these two algorithms.

A. FPS algorithm

The FPS algorithm [50] introduces an ancilla qubit to reproduce a non-unitary dynamics that damps out the oscillations of the results of Grover's algorithm between the target and non-target states. The algorithm uses a series of parametric rotations

$$R_y(\alpha_i) = \begin{pmatrix} \cos \frac{\alpha_i}{2} & -\sin \frac{\alpha_i}{2} \\ \sin \frac{\alpha_i}{2} & \cos \frac{\alpha_i}{2} \end{pmatrix}, \quad (5)$$

where the optimal value of the α_i angles depends on the specifics of the problem. The algorithm is presented in Fig. 2 and reads as follows

$$\Pi_{i=1}^K [(|0\rangle\langle 0| \otimes \mathbb{I} + |1\rangle\langle 1| \otimes \hat{R}_0)(R_y(-\alpha_i) \otimes \mathbb{I})] \quad (6)$$

$$(|0\rangle\langle 0| \otimes \mathbb{I} + |1\rangle\langle 1| \otimes \hat{O})(R_y(\alpha_i) \otimes \mathbb{I})] |1\rangle|\psi_0\rangle,$$

where the circuit is run a total number of K times depending on the result of a measurement performed on the ancilla qubit as we see next.

The first step of the algorithm rotates the ancilla qubit to $-\sin \frac{\alpha_i}{2}|0\rangle + \cos \frac{\alpha_i}{2}|1\rangle$. The second term performs a controlled operation which yields the state

$$|\Psi_1\rangle = -\sin \frac{\alpha_i}{2}|0\rangle|\psi_0\rangle + \cos \frac{\alpha_i}{2}|1\rangle(\cos\theta|\psi^\perp\rangle - \sin\theta|\psi_T\rangle). \quad (7)$$

The application of the second single-qubit rotation $R_y(-\alpha_i)$ leads to

$$\begin{aligned} |\Psi_2\rangle &= -\sin \alpha_i \sin \theta |0\rangle |\psi_T\rangle + \sin^2 \frac{\alpha}{2} |1\rangle |\psi_0\rangle \quad (8) \\ &+ \cos^2 \frac{\alpha}{2} |1\rangle (\cos \theta |\psi^\perp\rangle - \sin \theta |\psi_T\rangle) \\ &= -\sin \alpha_i \sin \theta |0\rangle |\psi_T\rangle - \cos \alpha_i \sin \theta |1\rangle |\psi_T\rangle \\ &+ \cos \theta |1\rangle |\psi^\perp\rangle. \end{aligned}$$

Now the action of the last controlled operation $(|0\rangle\langle 0| \otimes \mathbb{I} + |1\rangle\langle 1| \otimes \hat{R}_0)$ on $|\Psi_2\rangle$ is given by

$$\begin{aligned} |\Psi_3\rangle &= -\sqrt{p_{i+1}} |0\rangle (|\psi_T\rangle) \quad (9) \\ &+ \sqrt{1 - p_{i+1}} |1\rangle ((c_i \cos 2\theta - s_i \cos \alpha_i \sin 2\theta) |\psi^\perp\rangle \\ &+ (c_i \sin 2\theta + s_i \cos \alpha_i \cos 2\theta) |\psi_T\rangle), \end{aligned}$$

where we have used $p_{i+1} = \sin^2 \alpha_i \sin^2 \theta$, $c_i = \cos \theta$ and $s_i = \sin \theta$. Finally, depending on the outcome of the measurement performed on the ancilla qubit, we decide to stop or continue the algorithm. In fact, if we measure the state $|0\rangle$ on the ancilla qubit, the system collapses into the state $|\psi_T\rangle$. Conversely, if the outcome is $|1\rangle$, the system becomes a new superposition of the states $|\psi_T\rangle, |\psi^\perp\rangle$.

At the i -th repetition, the superposition state associated with $|1\rangle$ is

$$|\psi_{i+1}\rangle = c_{i+1} |\psi^\perp\rangle + s_{i+1} |\psi_T\rangle, \quad (10)$$

with the new coefficients defined as

$$\begin{aligned} s_{i+1} &= \frac{c_i \sin 2\theta + s_i \cos \alpha_i \cos 2\theta}{\sqrt{1 - p_{i+1}}} \quad (11) \\ c_{i+1} &= \frac{c_i \cos 2\theta - s_i \cos \alpha_i \sin 2\theta}{\sqrt{1 - p_{i+1}}} \end{aligned}$$

for $i = 1, \dots, K$ and

$$p_{i+1} = s_i^2 \sin^2 \alpha_i, \quad (12)$$

being the probability of measuring the ancilla qubit on $|0\rangle$.

Note that, depending on the choice for the sequence of the angles α_i , the instantaneous probability p_i may oscillates or even reduce at each iteration, but the cumulative probability p_{cum} , that is the probability of getting the outcome $|0\rangle$ at least once after after i iterations, is always non-decreasing. This is obtained by considering the probability of the complementary event, i.e. not measuring the desired outcome in the first i iterations.

$$p_{\text{cum}}(i) = 1 - \prod_{j=1}^i (1 - p_{j+1}) \quad \text{for } i = 1, \dots, K \quad (13)$$

The average number of oracle calls before success is given by:

$$\langle n_{\text{calls}} \rangle = \sum_i i \times [p_{i+1} \prod_{j=1}^{i-1} (1 - p_{j+1})], \quad (14)$$

where the term between squared brackets is the probability of having success exactly at the i -th iteration.

A sensible choice of the α_i leads the cumulative probability of success to rapidly grow to 1. In the case of knowing beforehand the value of M , and consequently of θ , the best choice is given by the constant critical value

$$\alpha_C = \arccos \left(\frac{1 - \sin 2\theta}{1 + \sin 2\theta} \right), \quad (15)$$

which has been found to be the optimal angle dampening the oscillations of Grover's algorithm between target and nontarget states[50]. When M is not known in advance but $M \ll N$, then the critical angle computed for $M = 1$ is an effective choice for a large set of values of M near 1. It is noteworthy to mention that the quantum counting algorithm has been proposed as a method to efficiently count the number of solutions that attain specific requirements of a given quantum search problem or simply counting the total number of solutions [59]. More recently, a new method has been proposed to estimate M by exploiting the relationship between this value and the probability of measuring one solution after a given number of iterations of the standard Grover's algorithm [60].

We show next, for the case of $M = 1$ and $N = 1000$, the evolution of the coefficients c_i, s_i together with the instantaneous and cumulative probabilities $p_i, p_{\text{cum}}(i)$ for different choices of α_i . In the case of using a constant critical angle, shown in Fig. 3c, the probability of success at each iteration p_i tends to increase. However, when the number of target states M is not known but it is supposedly very large, an effective choice is given by varying the angle in the following decreasing way

$$\alpha_1 = \pi/2, \quad (16)$$

$$\alpha_i = \arccos \left(\frac{1 - \sin(\pi/2i)}{1 + \sin(\pi/2i)} \right) \quad \text{for } i > 1, \quad (17)$$

for which the dynamics is plotted in Fig. 3d. In Fig. 3b, we compare the cumulative probabilities and the average number of oracle calls $\langle n_{\text{calls}} \rangle$ before success (vertical lines) for different choices of α (critical and decreasing) with the probability of classical random extraction (dashed line). Comparing the two different choices of α , the cost of not knowing M weights at most by a factor of 1.5 in the average number of oracle calls. Summing everything up, in Fig. 3a we compare the average number of oracle calls for the case $M = 1$ as a function of N for the critical and decreasing cases with respect to the references $\sqrt{N/M}$ and N/M . As expected, we find that the fixed point search algorithm has a scaling $\mathcal{O}(\sqrt{N/M})$, an improvement with respect to the classical $\mathcal{O}(N/M)$

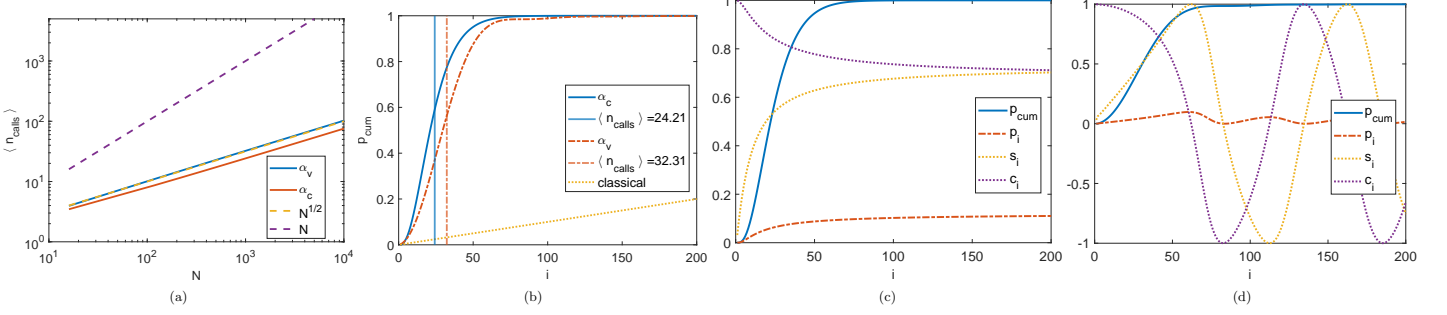


FIG. 3: In (a), the average number of oracle calls before success (using $M = 1$ and changing the database size N) for the constant critical value of $\alpha_C = \alpha_i$ and for the variable decreasing sequence, defined in (17) and referenced as α_V . This is compared with the references \sqrt{N} and N using a logarithmic scale on both the horizontal and vertical axes. The fixed point search algorithm provides a quadratic advantage with respect to classical search, for the considered angle's schedules. In (b), a comparison between the cumulative probabilities for the two choices with respect to a classical algorithm. The vertical lines represent the average number of queries to the oracle for the respective cases. In (c) and (d) the time evolution of the coefficients in Eq. (11), the instantaneous and cumulative probabilities p_i, p_{cum} for the case $M = 1, N = 1000$ with α_C and α_V respectively.

B. OAA algorithm

In order to apply either the Grover or the FPS algorithm, we need to know how to prepare the oracle \hat{O} as expressed in Eq. (2), which assumes some knowledge of the target state $|\psi_T\rangle$. Most of the times, we do not have all the pieces of information about the target state, but some of its values, which are stored in a subspace that labels if the quantum state is (or it is not) the target. Namely, we can think of a unitary operation \hat{U} such that

$$\hat{U}|0\rangle|\psi\rangle = |0\rangle V|\psi\rangle + |\Phi^\perp\rangle \quad (18)$$

where $|\psi_T\rangle = V|\psi\rangle$ has the label qubit set to $|0\rangle$ and $|\Phi^\perp\rangle$ is a state orthogonal to $|0\rangle|\psi_T\rangle$ with different value of the label qubit. The OAA algorithm allows the amplification of the state labeled by $|0\rangle$ regardless of the quantum state $|\psi_T\rangle$. This is a typical condition that we encounter in block-encoding algorithms [55] where the relevant dynamics is labeled by the $|0\rangle$ state.

We refer to the original paper [52] for the description of the algorithm. However, as a caveat, we remind that the OAA algorithm is exact only if the V operator is unitary [54], otherwise introducing errors into the target state.

IV. QUANTUM FRANS ALGORITHM

In this section we present our Quantum algorithm for the FRANS problem (QFRANS), which is obtained as an efficient and ad-hoc modification of the FPS algorithm. Later in this section we present a full analysis of each component of the quantum circuit.

We consider a dataset $\mathbb{X} = \{i, x_i\}_{i=1}^N$ which collects the label i given to N particles and the respective position

x_i . Our goal is to find all the pairs (i, j) such that the distance $d(i, j)$ is lower than the chosen fixed radius h .

The first part of the algorithm encodes two copies of the dataset in four quantum registers, by using bit-encoding. In particular, two quantum registers with $q_0 = \lceil \log_2 N \rceil$ qubits are used to encode the label of the particles, with the state $|i\rangle$ being the binary representation of the integer i , while q_1 qubits are used to encode their position by discretizing the whole space into a 2^{q_1} -points lattice, and letting the state $|x_i\rangle$ to represent the coordinates.

The preparation of the state is accomplished by employing the PREP operator, which acts on the position and label registers as

$$|\phi\rangle = \text{PREP}|0\rangle_{q_0}|0\rangle_{q_1} = \frac{1}{\sqrt{N}} \sum_i |i\rangle_{q_0} |x_i\rangle_{q_1}, \quad (19)$$

where the suffix given to the ket details the number of qubits. QFRANS applies PREP to both the particles register and label registers as

$$|\psi_0\rangle = \text{PREP} \otimes \text{PREP} |0\rangle_{q_0}|0\rangle_{q_1}|0\rangle_{q_0}|0\rangle_{q_1} = \frac{1}{N} \sum_{i,j} |i\rangle_{q_0} |x_i\rangle_{q_1} |j\rangle_{q_0} |x_j\rangle_{q_1}, \quad (20)$$

Once the dataset is encoded we evaluate the distance between all the points in the dataset $d_{ij} = d(x_i, x_j)$. This can be done by introducing a set a_1 of ancillary qubits initialized in $|0\rangle$ and by applying a generic distance operator \hat{D} on the two q_1 -qubits registers

$$|\psi_1\rangle = (\mathbb{I}_{2q_0} \otimes \hat{D})|\psi_0\rangle|0\rangle_{a_1} = \frac{1}{N} \sum_{i,j} |i\rangle_{q_0} |x_i\rangle_{q_1} |j\rangle_{q_0} |d_{ij}\rangle_{q_1} |0\rangle_{a_1}; \quad (21)$$

an efficient implementation of the operator \hat{D} in case of euclidean geometry is given in Sec. IV A 2.

The value $|\cdot\rangle_{a_1}$ of the ancilla qubits is not relevant at this stage of the calculation, but we cannot discard it as it will be useful later.

Once the state is prepared, according to Grover's algorithm and its FPS counterpart, now we construct the oracle operator that applies a negative phase to the states where $d_{ij} \leq h$.

Here resides the novelty of this work: we do not know what is our target state $|\psi_T\rangle$, so we do not aim to build the oracle operator as described in Eq. (2), nevertheless we build the oracle by constructing a diagonal operator which is able to invert the sign of all the possible solutions.

$$\hat{O}(h) = \text{diag} \left(\underbrace{-1, \dots, -1}_{h \text{ times}}, \underbrace{1, \dots, 1}_{2^{(q_1+1)} - h \text{ times}} \right). \quad (22)$$

When applied to $|\psi_1\rangle$ this yields

$$\begin{aligned} |\psi_2\rangle &= (\mathbb{I}_{2^{q_0+q_1}} \otimes \hat{O}(h) \otimes \mathbb{I}_{a_1}) |\psi_1\rangle \quad (23) \\ &= \sqrt{\frac{N-M}{N}} \sum_{d_{ij} > h} |i\rangle_{q_0} |x_i\rangle_{q_1} |j\rangle_{q_0} |d_{ij}\rangle_{q_1} |\cdot\rangle_{a_1} \\ &\quad - \sqrt{\frac{M}{N}} \sum_{d_{ij} \leq h} |i\rangle_{q_0} |x_i\rangle_{q_1} |j\rangle_{q_0} |d_{ij}\rangle_{q_1} |\cdot\rangle_{a_1} \\ &= \cos \theta |\psi^\perp\rangle - \sin \theta |\psi_T\rangle, \end{aligned}$$

where M is the number of neighboring pairs and in the last line of Eq. (23) we restored the convention that uses $|\psi^\perp\rangle$, $|\psi_T\rangle$ and the relative angle θ .

Finally we build the reflection over the initial state $|\psi_1\rangle$, \hat{R}_1 , similar to Eq. (3) as

$$\hat{R}_1 = 2|\psi_1\rangle\langle\psi_1| - \mathbb{I} = \hat{U}_1 (2|0\rangle\langle 0| - \mathbb{I}) \hat{U}_1^\dagger = \hat{U}_1 \bar{Z} \hat{U}_1^\dagger, \quad (24)$$

where we defined $\hat{U}_1 = \hat{D}\hat{U}$, and \bar{Z} as the expanded \hat{Z} operation which inverts the sign of the qubits different from $|0\rangle$. The application of \hat{R}_1 to the quantum state leads to $|\psi_3\rangle = \hat{R}_1|\psi_2\rangle$. Upon this premises, we are able to build the QFRANS algorithm as depicted in Fig. 4, which is analogue to the FPS algorithm, with an explicit state preparation for the FRANS problem, and a modified oracle operator. Although those differences, the result can be written as in Eq. (9), with

$$|\Psi_3\rangle = -\sqrt{p_{k+1}} \sqrt{\frac{M}{N}} \sum_{d_{ij} \leq h} (|0\rangle_{a_0} |i\rangle_{q_0} |x_i\rangle_{q_1} |j\rangle_{q_0} |d_{ij}\rangle_{q_1} |\cdot\rangle_{a_1}) \quad (25)$$

$$\begin{aligned} &+ \sqrt{1 - p_{k+1}} |1\rangle_{a_0} [(c_k \cos 2\theta - s_k \cos \alpha_k \sin 2\theta) \\ &\quad \sqrt{\frac{N-M}{N}} \sum_{d_{ij} > h} (|i\rangle_{q_0} |x_i\rangle_{q_1} |j\rangle_{q_0} |d_{ij}\rangle_{q_1} |\cdot\rangle_{a_1}) \\ &\quad + (c_k \sin 2\theta + s_k \cos \alpha_k \cos 2\theta) \\ &\quad \sqrt{\frac{M}{N}} \sum_{d_{ij} \leq h} (|i\rangle_{q_0} |x_i\rangle_{q_1} |j\rangle_{q_0} |d_{ij}\rangle_{q_1} |\cdot\rangle_{a_1})], \end{aligned} \quad (26)$$

In the remaining of this section we analyze each of the components of the algorithm separately.

A. State preparation

Here we describe the \hat{U}_1 operator needed to encode and process the pieces of information available in the database.

The fundamental premise of our algorithm relies on establishing a correspondence between dataset elements X_i and their integer representations x_i . When working with floating-point precision, this correspondence can always be achieved by defining a discretization grid based on the numerical precision of the computing system. More sophisticated grid selection schemes can be tailored to specific problem requirements and search radius ξ to optimize performance.

To identify and mark the target states that satisfy the proximity condition in Eq. (31), we must first determine the integer representation of the chosen distance threshold ξ . This conversion is feasible precisely because we have established a bit-encoding scheme that associates each dataset point with a unique integer value.

A critical requirement of our approach is that the input dataset must be evenly spaced, or equivalently, that the data space can be accurately described using a regular grid structure. Under this constraint, we can interpret the integer representation as the number of discrete distance units required to span the threshold distance ξ . For illustration, consider the one-dimensional case where this relationship is expressed as:

$$h = \left\lceil \frac{\xi}{\Delta x} \right\rceil, \quad (27)$$

where Δx represents the grid spacing. This discretization procedure effectively transforms the original continuous proximity problem into an equivalent integer formulation:

$$d(x_i, x_j) \leq h, \quad x_i, x_j, h \in \mathbb{N}. \quad (28)$$

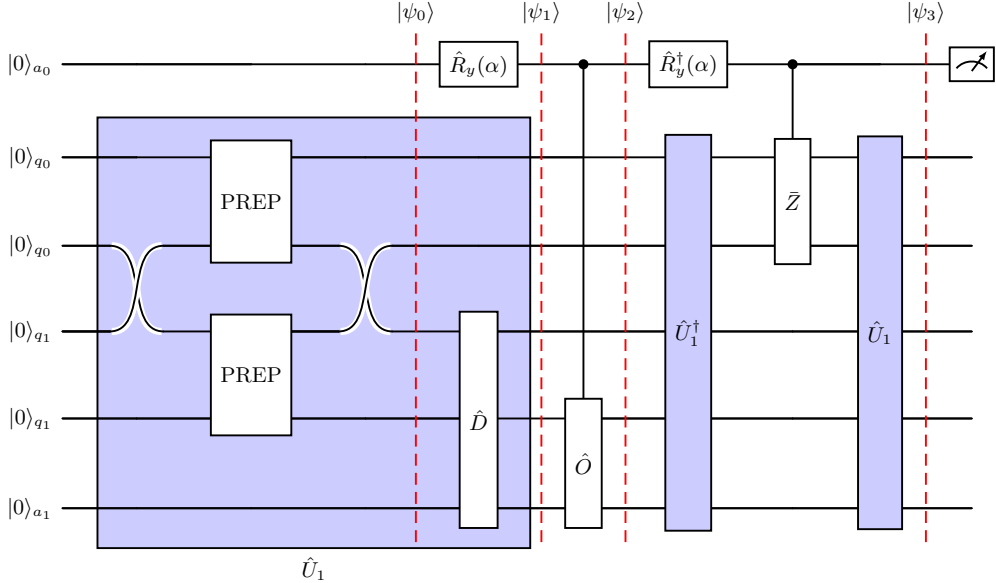


FIG. 4: The circuit for the QFRANS algorithm, which has to be repeated until the state measured in the register a_0 is $|0\rangle$.

Hence, We assume that both the label and the position of each particle are described by integers. Note that the ceiling function in Eq. (27) is suitable to a proximity condition that uses the inclusive inequality as in Eq. (28), whereas, for applications requiring a strict inequality, the floor function should favorable.

1. The PREP operator

In the following we treat PREP as a black-box operator that is able to prepare the state $|\phi\rangle$ as defined in Eq. (19). The construction of PREP is often disregarded but it is actually one of the hardest element to deal with. The quantum superposition of N states can be obtained by employing a circuit with depth $\mathcal{O}(N)$, thus exponential with the number of qubits q_0 of the label register [61, 62]. This can be interpreted as the sequential implementation of each particle directly on the quantum circuit, with the $\log N$ ancilla qubits facilitating the decomposition of multi-controlled gates. Note that by using the optimized algorithm of Ref. [61], we can implement PREP as two separate circuit, as shown in Fig. 5. The first operator, \hat{L} , defines the balanced superposition of N elements in the register with q_0 qubits $\hat{L}|0\rangle_{q_0} = \frac{1}{\sqrt{N}} \sum_{i=0}^{N-1} |i\rangle$. The second operator, \hat{E} , assigns to each particle its position, $\hat{E}|i\rangle_{q_0}|0\rangle_{q_1} = |i\rangle_{q_0}|x_i\rangle_{q_1}$.

This implementation of PREP allows us to use a reduced \hat{R}_1 operator, as we will see later.

One can drastically reduce the depth of the circuit by increasing its width, i.e. by employing ancilla qubits [63–65], an approach that culminates with a circuit that has width $\sim \mathcal{O}(N)$ while keeping the depth $\sim \mathcal{O}(\log N)$. This

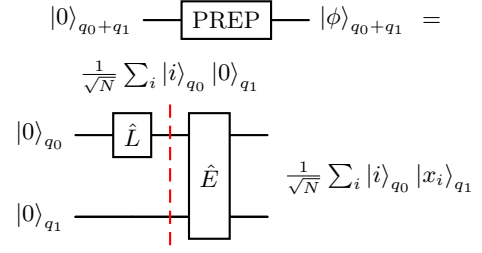


FIG. 5: A possible implementation of the PREP operator, where \hat{L} creates a balanced superposition of the labels of the particles and \hat{E} assigns to each particle its position.

constructs a register of N ancilla qubits containing the information for initial state preparation, effectively forming a database. Access to this repository scales logarithmically with the number of data points N , enabled by a tree-based data access structure. In our case, since the initial state has nearly uniform coefficients, the classical overhead for amplitude preparation is both constant and efficient. In general, different algorithms play with the tradeoff between depth and number of ancillas [64], while keeping the product depth \times width about constant. In order to build a functioning PREP operator, one should adapt the depth and the width to the specifics of the quantum computer available. Neither of the approaches at the extremes of this trade-off require all-to-all qubit connectivity; consequently, we do not expect connectivity constraints to significantly impact the algorithm's scaling.

Conversely, if the position of the particles follows some

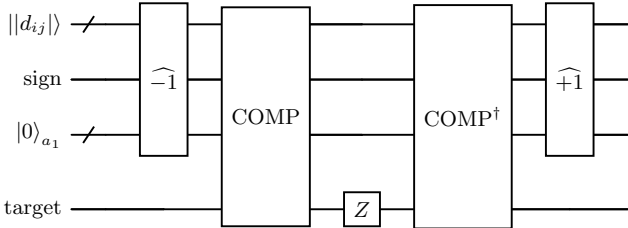


FIG. 6: Quantum Oracle. The circuit realizes the inverse oracle $-\hat{O}$ defined in Equation (31). It is important for the circuit to work correctly that the sign qubit is the most significant qubit. The target register stores the comparison result $d_{ij} \geq h$. The operators $\pm\hat{1}$ respectively add and subtract unity to the distance value; they can be implemented with a logarithmic depth quantum adder [68]. Removing the incrementer $\hat{+1}$ and decrementer $\hat{-1}$ operators recovers the expression in Equation (22). The original oracle \hat{O} can be recovered by replacing the Z gate with $-Z$.

structure, that is it can be described by a mathematical function, we can use matrix access oracles with depth $\sim \mathcal{O}(\text{poly log } N)$ [65–67].

2. The distance operator \hat{D}

In a generic scenario, the distance operator \hat{D} is applied on a combination of two identical states superpositions $|\phi\rangle|\phi\rangle$

$$\hat{D} \sum_{i,j} |x_i\rangle_{q_1} |x_j\rangle_{q_1} |0\rangle_{a_1} = \sum_{i,j} |x_i\rangle_{q_1} |d_{ij}\rangle_{q_1+1} |0\rangle_{a_1-1}, \quad (29)$$

where $|d_{ij}\rangle_{q_1+1}$ is the state encoding the signed distance between the particle x_i and x_j . The extra qubit $q_1 + 1$ is borrowed from the ancillary register and used to represent the sign of the distance.

Consider a three-dimensional Euclidean space with L_2 distance $d(r_i, r_j) = \sqrt{(x_i - x_j)^2 + (y_i - y_j)^2 + (z_i - z_j)^2}$. The integer FRANS problem in Eq. (28) reduces to identifying particle pairs contained within a sphere of radius h . However, in certain scenarios, such as cosmological simulations [9], it is sufficient to determine whether particles fall within a cube of side length h (Chebyshev distance). This approach decomposes the problem into three independent one-dimensional searches along each Cartesian axis, where the distance equals the absolute difference of the coordinates.

$$d(r_i, r_j) \leq \epsilon \mapsto |x_i - x_j| \leq h \wedge |y_i - y_j| \leq h \wedge |z_i - z_j| \leq h. \quad (30)$$

Henceforth, we focus on the one-dimensional case, as the problem reduces to this simpler scenario when employing the Chebyshev distance.

Before delving into details regarding the implementation of the absolute difference, we must explain how negative integers are represented in binary. Negative integer values are represented in binary form using two's complement: the binary representation of the integer is negated and 1 is added, with the most significant bit (MSB) encoding the sign. For example, consider the integer 10 with binary representation 01010. We first negate the value to obtain 10101, then add 1 to yield 10110, the binary representation of -10 . To recover the absolute value of a negative integer, we apply two's complement again: negate the bits to obtain 01001, then add 1 to recover 01010, corresponding to 10. Thus, obtaining the absolute value requires negation followed by adding 1 when the distance is negative.

In a quantum circuit, the difference between two binary values a and b is computed using the inverse Ripple Carry Adder [69], which requires $\mathcal{O}(q_1)$ CNOT gates and only 2 ancilla qubits: one for the carry of the subtraction and another as a clean ancillary qubit. When $a > b$, the carry qubit remains in state $|0\rangle$ and yields the correct result. When $a < b$, the carry qubit flips to $|1\rangle$, producing the two's complement representation of $a - b$. We thus treat the carry bit as the sign qubit and effectively as part of the distance.

To obtain the absolute value, when the sign qubit is $|1\rangle$, the incrementer $\widehat{+1}$ is applied to the distance register, performing the addition of unity: $\widehat{+1}|d_{ij}\rangle = |d_{ij} + 1\rangle$. This controlled incrementer can be implemented with circuit depth $\mathcal{O}(q_1)$ [68, 70]. Subsequently, the value is negated via a series of q_1 $CNOT$ gates, each controlled by the sign qubit and acting on $|d_{ij} + 1\rangle$.

However, instead of using the absolute difference between particles, we propose to work with the signed difference. The negative values will be then disregarded as non-target states by an appropriate choice of the oracle; this will be explained in Sec **IV B**. This operation is considerably simpler, requiring only the inverse adder and avoiding the controlled operations. Moreover, the number of target states is reduced by half, as each pair is counted only once.

Summing up, the choice of the Chebyshev distance over the L_2 norm reduces the overall depth of the distance operator \hat{D} , as it allows the use of signed differences along each spatial dimension. In this context, \hat{D} comprises three inverse adder operators, one acting along each spatial coordinate. This eliminates the squaring and summing operations required by the Euclidean distance [42], thereby reducing the overall complexity of the distance operator.

B. The oracle \hat{O}

The oracle presented in Equation (22) represents the most naive implementation, as it incorporates elements with zero distances. This becomes particularly valuable when different particles are mapped to identical positions

due to finite precision constraints. It is also the cheapest option in terms of ancilla qubits, number of CNOT and circuit depth.

The most direct approach to implementing the oracle \hat{O} employs the diagonal decomposition method described in Reference [71]. However, this approach exhibits unfavorable scaling properties, with both the number of CNOT gates and circuit depth scaling as $\mathcal{O}(2^{q_1+1})$, rendering it impractical for large-scale implementations.

An alternative approach would be to implement the oracle as a series of multi-controlled Z gates (MCZ). In this scenario, we would require $\mathcal{O}(h)$ MCZ gates. Using the approach described in [72, 73] the global scaling of the oracle would be $\mathcal{O}(hq_1)$.

We can achieve a substantial improvement, reducing the complexity to $\mathcal{O}(q_1)$, by exploiting the inherent structure of our problem. In fact, we propose an oracle implementation that utilizes an integer comparator circuit (COMP), which requires $q_1 - 1$ clean ancilla qubits and one additional qubit to store the comparison result $d_{ij} \geq h$. When this condition is satisfied, the target qubit is found in state $|1\rangle$. The comparator's operation can be formally expressed as $\text{COMP}\left(\sum_{ij} |d_{ij}\rangle_{q_1+1} |0\rangle\right) = \sum_{ij} |d_{ij}\rangle_{q_1+1} |d_{ij} \geq h\rangle$. Choosing the most significant qubit as the sign bit, we set up a natural filtering mechanism. By adopting this choice, when we have a negative distance d_{ij} , the sign qubit is set to $|1\rangle$, which automatically makes the entire numerical value at least 2^{q_1} . Since all negative values are now greater than $2^{q_1} - 1$, the comparator naturally excludes them without any additional circuit. This elegant consequence of our sign bit placement simplifies the overall implementation.

To optimize circuit complexity, we implement the inverse oracle $-\hat{O}$ rather than the oracle defined in Equation (22). This is achieved through a phase kickback mechanism: we first apply the quantum comparator to the distance register, then apply a Z gate to the comparator's target qubit, and finally reset the target qubit to $|0\rangle$ by applying COMP^\dagger . This procedure introduces a negative phase to all elements whose distance satisfies $d_{ij} \geq h$. Using this approach the Oracle requires only q_1 clean ancilla qubits.

However, when one is faced with large datasets, e.g., $N = 10^9$ particles, we suggest to employ a slightly different oracle

$$\hat{O}(h) = \text{diag}\left(1, \underbrace{-1, \dots, -1}_{h-1 \text{ times}}, \underbrace{1, \dots, 1}_{2^{(q_1+1)-h} \text{ times}}\right). \quad (31)$$

where we introduced a modification to exclude zero-distance values $|0\rangle$. This eliminates comparisons between identical data points, reducing the number of solutions by N . In practical applications, e.g., cosmological simulations where $N \sim 10^{10}$, this optimization provides significant computational advantages.

Figure 6 illustrates the quantum circuit implementation of $-\hat{O}$ from Equation (31). Zero values are excluded

from the marked states by replacing the standard comparator COMP with $\text{COMP}(\widehat{-1})$, where $\widehat{-1}$ represents the inverse quantum incrementer based on a logarithmic depth quantum adder [68]. To maintain linear scaling in both CNOT count and circuit depth with respect to q_1 , this modified approach requires $2q_1 - \log_2 q_1$ clean ancilla qubits [70], which allows us to use the same ancilla qubits for both the comparator and the incrementer.

In Fig. 7 we show a comparison of the depth and number of ancilla qubits required to implement both version of the oracle. We have to consider also that the fewer the number of target states M , the harder is to find them. Specifically the number of required repetition is expected to scale as $\mathcal{O}(N/\sqrt{M})$ (cf. Sec III, as N^2 is the number of all the possible pairs of the dataset with N elements.

C. The reflection

The final step of the QFRANS algorithm requires performing an inversion around the initial state $|\psi_1\rangle$. As demonstrated in Eq. (24) and illustrated in Figs. 4–8, this can be achieved through the implementation of a single operator \bar{Z} .

To maintain consistency with our circuit optimization strategy introduced in Section IV B, where we implemented the negative oracle $-\hat{O}$ rather than the positive version, we adopt the same approach here by constructing $-\hat{R}_1$ instead of \hat{R}_1 . This design choice ensures that the accumulated negative phases from both the oracle and reflection operators cancel out, ultimately producing results that are identical to the standard implementation presented in Section IV. Under this modified framework, the required operator becomes $-\bar{Z} = \mathbb{I} - 2|0\rangle\langle 0|$, which can be efficiently realized as a multi-controlled Z gate that activates when all control qubits are in the $|0\rangle$ state.

Figure 8 presents an explicit representation of the R_0 implementation. As established in Section IV A 1 and illustrated in Figure 5, PREP can be factorized as the product of label creation operator \hat{L} and element creation operator \hat{E} . Consequently, following application of \hat{Z} , the complete \hat{U} operator need not be applied in all cases. When readout measurements target only the labels of dataset elements, applying \hat{L} suffices to create the particle labels, whereas \hat{U} would reconstruct a superposition of particle elements and distances. However, when the ancilla measurement yields $|1\rangle$, correct algorithmic behavior requires the full \hat{U} operator. This is achieved by applying the remaining components \hat{E} and \hat{D} to the appropriate registers.

The scaling of \hat{R}_0 is dominated by the PREP operator. In fact, [73] shows that it is possible to implement a multi-controlled X gate using only $12n + \mathcal{O}(1)$ qubits and one dirty ancilla, where in the QFRANS scenario $n = 2q_0$. Consequentially, even with an advantageous decomposition of the MCZ, the implementation of \hat{R}_0 remains the bottleneck of the algorithm, as the depth and complexity scales in the same manner as PREP.

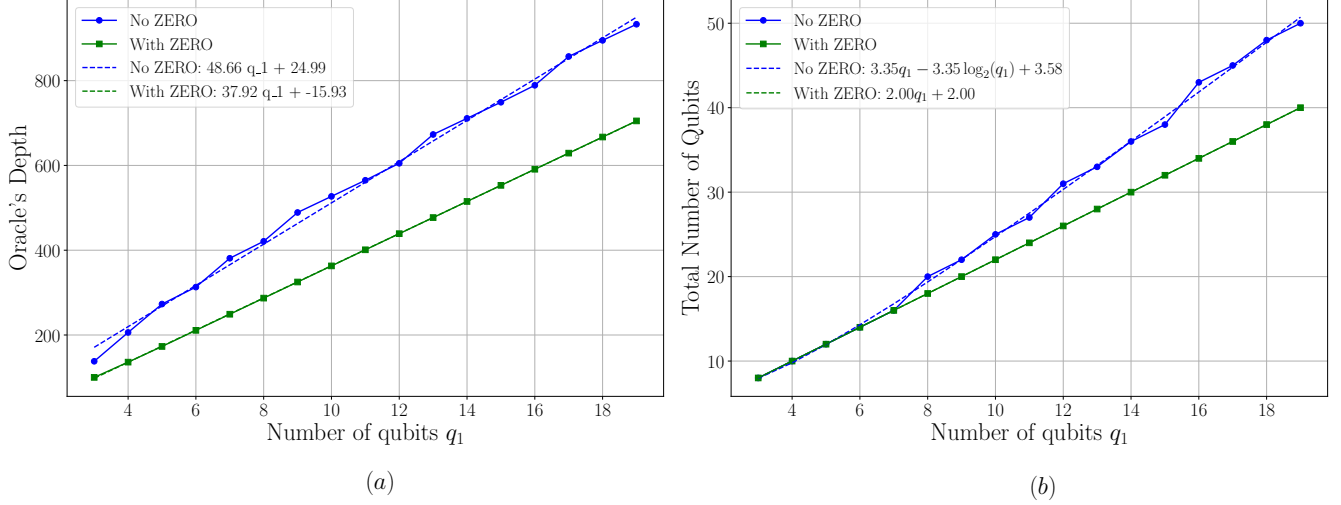


FIG. 7: Depth (a) and total number of qubits (b) as a function of the number of qubits q_1 . The green line refers to the oracle built using the comparator for the case including Zero as in Eq. (31)); the blue line to the case without zero as in Eq. (22).

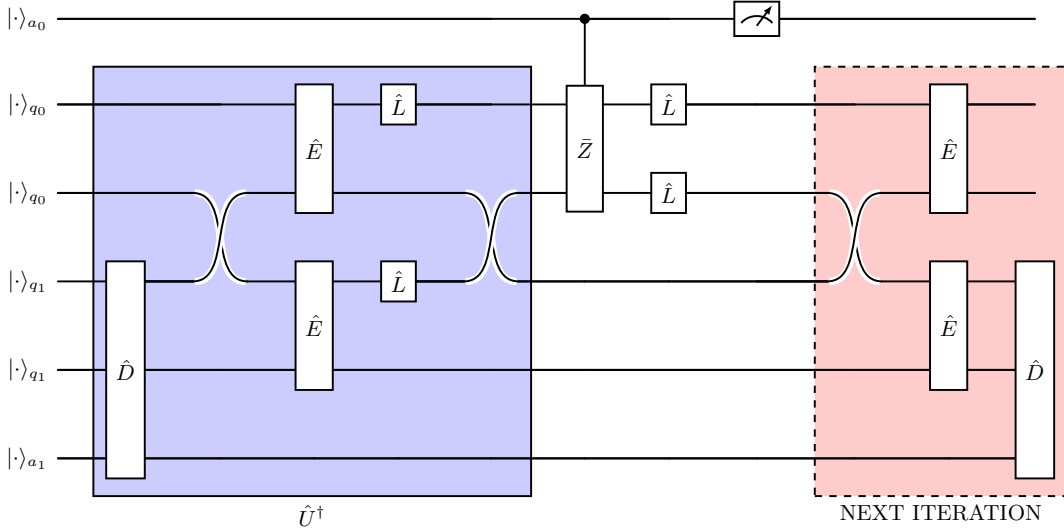


FIG. 8: Explicit representation of the \hat{R}_0 operator. The part included by the red-dashed line is applied only if the ancilla measurement is $|1\rangle$.

D. The readout measurement

The protocols described in Sec. IV B and Sec. IV C have to be repeated until we measure the state $|0\rangle_{a0}$ on the ancilla qubit. When this happens, supposing an error-free quantum hardware, the system has collapsed to the target state, an uniform superposition of the M solutions.

We propose to use the Bayes rule to estimate the value M representing the number of solution states. We treat M as a random variable and assume, under the hypoth-

esis $N \gg M$, a Poisson prior probability distribution

$$p(M) = \frac{\mu^M e^{-\mu}}{M!}, \quad (32)$$

with the mean number of solutions' pairs $\mu = \sum_M M p(M)$. The initial value for μ can be derived from previous simulation results or a priori knowledge of the problem (e.g., statistical information from classical simulations). In the absence of such prior knowledge, we set μ to the expected number of neighboring pairs in a uniform particle distribution $(\frac{2h}{L})^d N^2$.

The probability that in a FRANS problems with

M solutions, the QFRANS algorithm converges to the target state after m queries is given by the probability of failure in the first $m-1$, combined with success at the m -th one: $p_0(m|M) = p_m(M) \prod_{i=1}^{m-1} (1 - p_i(M))$. Here $p_i(M)$ and $p_m(M)$ are functions of M , and their expression is given in Eq. (12). The dependence on M is hidden in the θ coefficients of Eq. (11), explicitly $\theta = \arcsin \sqrt{M/N}$. When after m oracle's queries the ancilla is measured in state $|0\rangle$, the algorithm has converged to the solution. Following the readout measurements, the prior distribution is updated accordingly to the Bayes rules

$$p(M|m) = \frac{p_0(m|M) \times p(M)}{\sum_M' p_0(m|M') p(M')} . \quad (33)$$

Using the probability in Eq. (33) is possible to obtain a better estimate of the number of solutions $\mu = \sum_M M p(M|m)$. This updated value provides a principled basis for establishing an upper bound on the number of oracle queries. Since the algorithm is expected to converge in $\mathcal{O}(\sqrt{N^2/M})$ iterations, and μ serves as an estimate of M , we can set the iteration limit to $\mathcal{O}(\sqrt{N^2/\mu})$.

To determine when the QFRANS sampling procedure should stop, we adopt a Bayesian stopping criterion based on the probability of observing new solutions. Using the updated posterior distribution in Eq. (33) the probability that the next sample will reveal a previously unseen solution:

$$P_{\text{new}} = \mathbb{E}_{M|\text{data}} \left[1 - \frac{K}{M} \right] = \sum_{M=k}^N p(M, m) \left(1 - \frac{K}{M} \right), \quad (34)$$

where K is the number of distinct solutions observed thus far. This criterion directly reflects the operational goal of determining whether further QFRANS iterations are likely to yield new information. The algorithm stops when P_{new} falls below an arbitrary threshold: $P_{\text{new}} < \varepsilon$.

V. NUMERICAL TESTS

We have run simulations to verify the behavior of QFRANS and the stopping criterion under different conditions. We considered a 1 dimensional setup, where 6 particles are arranged in a box of dimension $L = 8$: $\mathbf{x} = \{0; 1; 3; 4; 6; 7\}$. We first choose an integer smoothing length $h = 1$ such that $M = 3$ with neighboring result couple being $(x_0, x_1); (x_2, x_3); (x_4, x_5)$. Figure 9 illustrates the interplay between the prior mean μ and convergence tolerance ε (Eq. (34)) in determining the probability of recovering all correct solutions. For a given ε , underestimating μ accelerates convergence at the risk of missing solution pairs, while overestimating μ ensures complete recovery but requires smaller ε values and incurs higher computational costs through increased oracle queries. Our analysis reveals that $\varepsilon = 10^{-2}$ strikes an

effective balance, guaranteeing robust convergence provided the initial mean is not severely underestimated. This behavior is consistent across both $M = 3$ and $M = 5$ cases, as shown in Fig. 10, although simulations with $\mu = 16$ reach the maximum iteration limit of 30 before achieving convergence.

A key finding is that complete solution recovery remains possible even when the probability distribution $p(M)$ fails to converge to a sharp peak around the true value. This robustness arises directly from our convergence criterion (Eq. (34)), which validates solutions through an independent mechanism rather than relying solely on the estimated mean.

Moreover, to better assess how the choice of μ and ε affects both the convergence rate and the number of solutions found, we ran a series of tests. Specifically, fixing $M = 5$, we performed nine simulations for each (μ, ε) configuration in order to compute the average number of iterations and the average number of solutions recovered. We repeated this procedure for two settings: one in which the maximum number of allowed queries was 3, and another in which it was 5.

From the results reported respectively in Tabs. I and II, we observe that restricting the number of queries tends to increase the likelihood of finding all solutions at the cost of slower convergence. Conversely, allowing too many queries can drastically reduce the probability of recovering all solutions under the same (μ, ε) configuration. This occurs because the probability in Eq. (33) depends on the likelihood of obtaining a measurement within m queries: larger m speeds up convergence but reduces accuracy, namely, the ability to recover all solutions.

Moreover, recalling that the algorithm converges in $\mathcal{O}(\sqrt{N^2/M})$ queries, we point out how in this case such value correspond to approximately $\sqrt{36/5} \simeq 3$. This value thus represents the ideal threshold for allowed queries. However, the true value of M is not known a priori and only have its estimate or guess μ is available. Thus, to provide a more standardized and broadly applicable procedure, we repeated the simulations where the maximum number of queries adapted to the estimated mean value μ , according to

$$\left\lceil 1.5 \sqrt{\frac{N^2}{\mu}} \right\rceil . \quad (35)$$

From the results presented in Tab. III is clear that the key requirement for finding all solutions is to overestimate the true number of solutions. The choice $\varepsilon = 10^{-2}$ appears to offer a good compromise between convergence speed and the possibility of finding all solutions, even when the overestimation is modest.

VI. ANALYSIS OF NOISE RESILIENCE

Today's quantum hardware is affected by noise and implementing any search algorithm in a scalable system is a

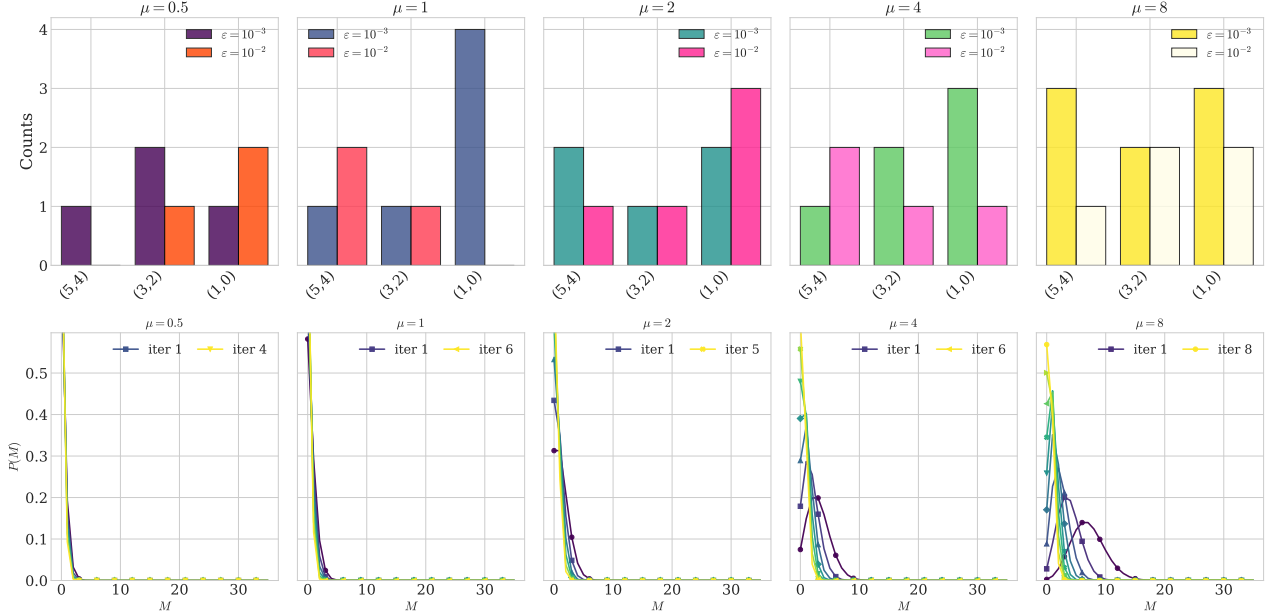


FIG. 9: Results from simulation with $N = 36$, $M = 3$ and 5 maximum queries allowed per run. The results are presented for different initial mean guesses μ in the prior distribution of Eq. (32). In the top row is shown the outcome of the readout, listing name of the particles on the x axis and their respective occurrences for different stopping tolerance ε . In the bottom row the evolution of the prior probability in Eq. (33) as a function of M , in the case where $\varepsilon = 10^{-3}$.

TABLE I: Mean number of iteration and found solutions as a function of the tolerance for the stopping criterion ε and estimated number of solutions μ . The results are obtained using 3 maximum allowed queries and the means and errors are evaluated on a sample of 9 data.

μ	$\varepsilon = 10^{-1}$		$\varepsilon = 10^{-2}$		$\varepsilon = 10^{-3}$		$\varepsilon = 10^{-4}$	
	Solution	Iteration	Solution	Iteration	Solution	Iteration	Solution	Iteration
0.5	2.0 ± 0.0	2.0 ± 0.0	3.0 ± 0.0	3.6 ± 0.6	4.0 ± 0.0	7.3 ± 1.0	5.0 ± 0.0	12.6 ± 3.7
2	3.0 ± 0.0	3.2 ± 0.3	4.3 ± 0.4	9.0 ± 1.5	5.0 ± 0.0	12.4 ± 2.2	5.0 ± 0.0	22.3 ± 0.77
8	4.6 ± 0.4	10.7 ± 1.6	5.0 ± 0.0	16.3 ± 0.8	5.0 ± 0.0	29.0 ± 0.0	5.0 ± 0.0	30.0 ± 0.0
16	5.0 ± 0.0	11.4 ± 1.0	5.0 ± 0.0	24.0 ± 0.0	5.0 ± 0.0	30.0 ± 0.0	5.0 ± 0.0	30.0 ± 0.0

significant challenge [74, 75]. Only recently, a novel noise tolerant method has been developed to reduce the error threshold for Grover's search by optimizing the number of iterations [76].

In this section we employ a simple model in order to analyze the effect of the noise on the result of the QFRANS algorithm assuming to have a quantum computer that can be characterized only by a bit-flip readout error. This assumption, though quite restrictive, can be used to characterize the noise resilience of the proposed algorithm. Therefore, we consider that the state, after successful measurement of the ancilla qubit onto $|1\rangle$, has collapsed into the correct target state $|\psi_T\rangle$ and that noise affects the algorithm only in the readout measurement part. We will see that this assumption does not change our proposed strategy which does not rely on error cor-

rection codes.

The bit-flip channel noise flips the state of a qubit with a probability $1-p = \text{error rate}$, where p is the probability of getting the correct result. This error can affect the two registers that are actually measured, both with q_0 qubits, which give the labels corresponding to the two particles. Starting from the states $|i\rangle_{q_0}, |j\rangle_{q_0}$, the overall probability of successfully measuring the exact indexes i and j is given by p^{2q_0} . As a result, if we set a tolerance value TOL for this probability, i.e. $p^{2q_0} \geq \text{TOL}$, the error rate must satisfy the following inequality:

$$\text{error rate} \leq 1 - \text{TOL}^{\frac{1}{2q_0}}. \quad (36)$$

Using reasonable values for the tolerance $\text{TOL} = 0.99$ and the number of qubits $q_0 = 30$ to encode a large database of $N = 2^{30}$ particles, the required error rate is in the order

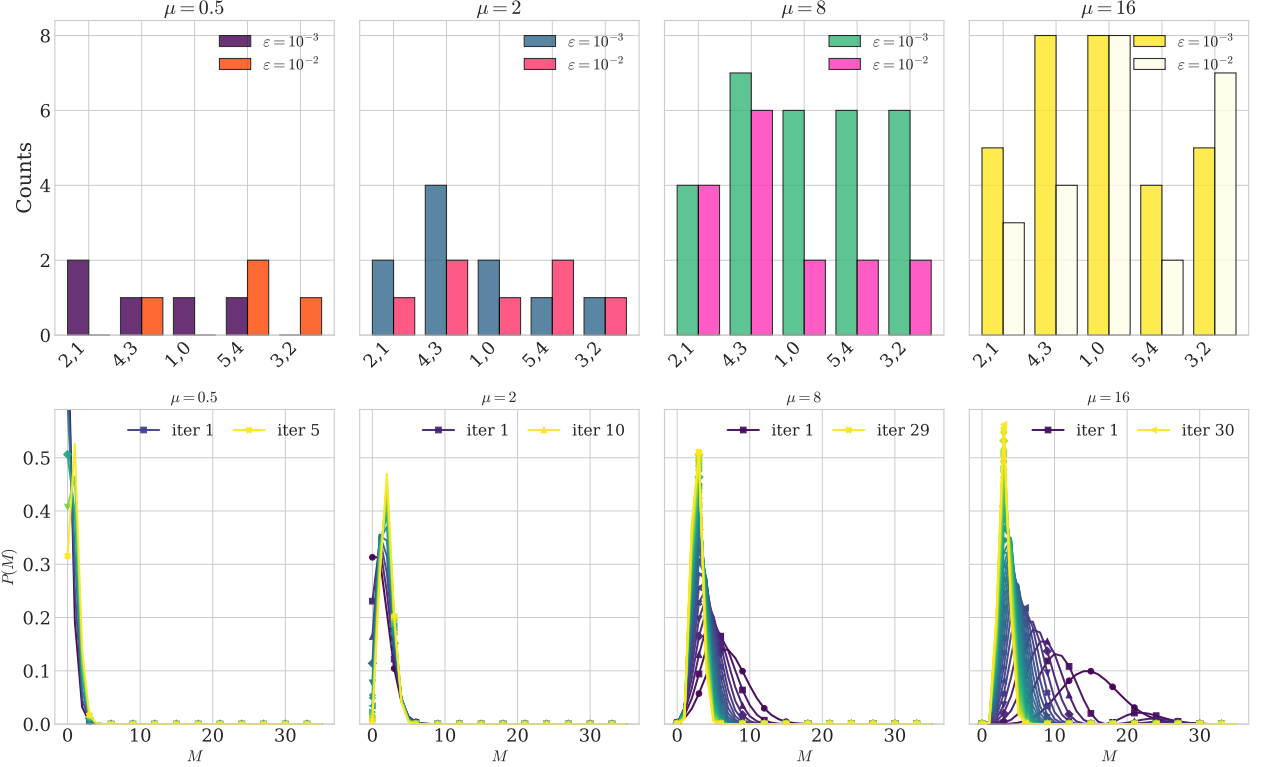


FIG. 10: Results from simulation with $N = 36$, $M = 5$ and 3 maximum queries allowed per run. The results are presented for different initial mean guesses μ in the prior distribution of Eq. (32). In the top row is shown the outcome of the readout, listing name of the particles on the x axis and their respective occurrences for different stopping tolerance ϵ . In the bottom row the evolution of the prior probability in Eq. (33) as a function of M , in the case where $\epsilon = 10^{-3}$. For both set of simulations the maximum number of allowed iteration is 30.

TABLE II: Mean number of iteration and found solutions as a function of the tolerance for the stopping criterion ϵ and estimated number of solutions μ . The results are obtained using 5 maximum allowed queries and the means and errors are evaluated on a sample of 9 data.

μ	$\epsilon = 10^{-1}$		$\epsilon = 10^{-2}$		$\epsilon = 10^{-3}$		$\epsilon = 10^{-4}$	
	Solution	Iteration	Solution	Iteration	Solution	Iteration	Solution	Iteration
0.5	1.0 ± 0.0	1.0 ± 0.0	2.0 ± 0.0	2.3 ± 0.5	2.9 ± 0.3	4.0 ± 0.6	3.0 ± 0.0	3.7 ± 0.9
2	2.0 ± 0.0	2.4 ± 0.6	2.9 ± 0.3	4.0 ± 0.7	3.1 ± 0.3	4.8 ± 1.1	3.4 ± 0.4	5.6 ± 0.8
8	2.7 ± 0.4	3.9 ± 0.8	3.2 ± 0.3	5.2 ± 0.8	3.6 ± 0.4	6.7 ± 1.1	4.4 ± 0.4	6.8 ± 0.8
16	3.7 ± 0.4	4.9 ± 0.5	3.8 ± 0.5	6.4 ± 0.6	4.6 ± 0.4	7.6 ± 0.4	4.4 ± 0.6	9.3 ± 0.8

TABLE III: Mean number of iteration and found solutions as a function of the tolerance for the stopping criterion ϵ and estimated number of solutions μ . The results are obtained using an iterative maximum number of queries that adapts to the estimate of μ . The means and errors are evaluated on a sample of 9 data.

μ	$\epsilon = 10^{-1}$		$\epsilon = 10^{-2}$		$\epsilon = 10^{-3}$		$\epsilon = 10^{-4}$	
	Solution	Iteration	Solution	Iteration	Solution	Iteration	Solution	Iteration
0.5	1.0 ± 0.0	1.0 ± 0.0	1.0 ± 0.0	1.0 ± 0.0	2.0 ± 0.0	2.2 ± 0.3	2.0 ± 0.0	2.4 ± 0.6
2	1.8 ± 0.3	2.0 ± 0.0	2.0 ± 0.0	2.0 ± 0.0	2.3 ± 0.3	3.1 ± 0.3	2.9 ± 0.3	3.6 ± 0.6
8	3.3 ± 0.4	4.2 ± 0.3	3.9 ± 0.3	5.4 ± 0.4	4.1 ± 0.3	6.1 ± 0.3	3.9 ± 0.6	6.6 ± 0.4
16	4.2 ± 0.5	7.3 ± 0.7	4.7 ± 0.4	9.2 ± 1.0	4.8 ± 0.3	10.3 ± 0.4	4.8 ± 0.3	11.4 ± 0.56

of 10^{-4} . Within this simplified model, the proposed algorithm provides sufficiently accurate results within currently available error rates. To improve the robustness of the proposed algorithm to noise, post-readout classical measurement techniques can be employed. For instance, if the full reflection operator is applied at the last iteration, measuring the state of the distance register q_1 provides a direct method for error detection: an error has occurred if the measured distance exceeds the integer smoothing length h . Moreover, a mismatch between the position register q_1 and the label of the first particle can also reveal erroneous circuit behavior, indicating that the readout should be rejected.

VII. DISCUSSION AND CONCLUSIONS

One of the main bottleneck in N-body methods is the FRANS subroutine. This is due to cache misses that arise when data that are close in space resides in distant memory locations. In this work we explored a possible solution using quantum computers. We emphasize that our goal was not to compete with state-of-the-art classical methods, but rather to introduce quantum algorithms aimed at finding alternative solutions to a class of problems that classically suffer from cache misses. We regard the present work as a preliminary step in a direction that may draw significant benefits from future developments of quantum computing.

Building on fixed point amplitude amplification we developed QFRANS, a quantum algorithm that finds all the elements whose distance is less than a fixed radius ξ with the use of an ancilla qubit that signals if the quantum state has reached the target. We developed an explicit encoding of the data that, by leveraging quantum superposition, simultaneously evaluates all the N^2 distances between particles. This allows to recover with $\mathcal{O}(M \log M)$ measures and a single quantum circuit all the pairs of close neighbors, as opposed to classical FRANS algorithms that repeat the search process for each particle with the risk of incurring in cache miss. One of the novelty of this work resides in the *oracle*, which is efficiently implemented on a quantum circuit by using two comparators and with a depth scaling linearly with the number of qubits. We proposed two different versions of such oracle, that can be used in different scenarios. We introduced the possibility of using the Chebyshev distance in place of the Euclidean one, bringing the complexity of the oracle to $\mathcal{O}(q_1)$ where 2^{q_1} is the number of grid points used to discretize one dimension. Our algorithm is robust against bit-flip errors in the readout measurements process thanks to the encoding of data labels and distances that allows an easy-to-implement error detection. We proposed and tested on a 1D simulation an efficient stopping criterion based on classical Bayes interference.

We found that the probability and speed of recovering all solutions also depend on the maximum number of

queries allowed. We propose an adaptive strategy that sets this threshold based on the estimation of M . Our observations show that with a tolerance value of $\varepsilon = 10^{-2}$, this approach provides a good compromise between the number of iterations and the recovery of all neighboring particles, provided that M is over-estimated.

Even though we employed state of the art algorithms, state preparation represents the major contribution to the circuit depth of our algorithm. For unstructured datasets, current methods face a fundamental depth-width trade-off: implementations requiring $\mathcal{O}(N)$ circuit depth utilize $\mathcal{O}(\log N)$ ancilla qubits, while those achieving $\mathcal{O}(\log N)$ depth demand $\mathcal{O}(N)$ ancilla qubits. Intermediate strategies exist between these extremes, though all maintain the constraint $\text{depth} \times \text{width} = \mathcal{O}(N \log N)$.

The fixed-point algorithm necessitates $\sqrt{N^2/M}$ queries to achieve the target state, which, when combined with the cost of implementing the oracle and diffusion operator, yields overall depth $\mathcal{O}(M^{-1/2}N^2)$ with $\mathcal{O}(\log N)$ ancilla qubits, or $\mathcal{O}((M \log M)^{1/2}N \log N)$ depth with $\mathcal{O}(N)$ ancilla qubits, depending on the encoding protocol. In addition we need to account for the readout requiring $\mathcal{O}(M \log M)$ measurements. Although at first glance the computational complexity of QFRANS does not appear to offer substantial advantages over the best classical methods ($\mathcal{O}(N \log N)$), a couple of considerations should be weighed before drawing firm conclusions. The first concerns cache-misses in classical FRANS codes. This issue primarily slows down execution time because the volume of data the CPU must process is too large to be kept in cache and therefore resides in RAM. The classical codes are then heavily parallelized to reduce the amount of data streamed to the CPU, which shortens run times and lowers overall complexity.

By analogy, the main obstacle to implementing QFRANS is the enormous cost of state preparation. In particular, choosing to work with $\mathcal{O}(N)$ ancilla qubits and depth $\mathcal{O}(\log N)$ is equivalent to having a particles' database with logarithmic access. If one were to parallelize the algorithm, the load on the QPU would decrease, making an implementation more plausible. Once again, QFRANS does not suffer from cache misses as there is no QRAM [77] and the burden falls entirely on the QPU. This will be analogous to a classical cache-only implementation. Nevertheless, the limiting factor here is still the sheer amount of data, thus for the moment, QFRANS should be regarded as a proof of concept, as well as a cache only classical implementation.

In future research more efficient state preparation algorithms will be investigated. As anticipated, a more detailed study on domain decomposition strategies may offer computational advantages, though at the cost of requiring multiple circuit implementations. Additionally, detailed studies of specific applications, such as cosmological simulations or molecular dynamics as well as flows on dynamic porous media may be used to validate the algorithm's practical utility. Understanding error propagation and developing robust mitigation strategies will

be considered in future studies. QFRANS represents a promising foundation for quantum algorithms addressing neighbor search problems. This work suggests that quantum computing may offer genuine advantages in computational domains where classical methods face fundamental memory hierarchy limitations rather than purely algorithmic constraints.

ACKNOWLEDGMENTS

We thank Simona Perotto, Filippo Marchetti, Stefano Borgani and Luigi Iapichino for valuable discussions. LC and GM have benefited scientifically from the collaboration with the Spoke 10 INAF group. LC, GM, CS and SS acknowledge financial support from the Italian National Center for HPC, Big Data and Quantum Computing (CN00000013).

[1] J. Klinkenberg, A. Kozhokanova, C. Terboven, C. Foyer, B. Goglin, and E. Jeannot, H2m: Exploiting heterogeneous shared memory architectures, *Future Generation Computer Systems* **148**, 39 (2023).

[2] B. Drávai and I. Z. Reguly, Performance and efficiency: A multi-generational benchmark of modern processors on bandwidth-bound hpc applications, *Future Generation Computer Systems* **169**, 107793 (2025).

[3] J. Feder, E. G. Flekkøy, and A. Hansen, *Physics of flow in porous media* (Cambridge University Press, 2022).

[4] M. Sahimi, Flow phenomena in rocks: from continuum models to fractals, percolation, cellular automata, and simulated annealing, *Reviews of modern physics* **65**, 1393 (1993).

[5] A. Cali, S. Succi, A. Cancelliere, R. Benzi, and M. Gramignani, Diffusion and hydrodynamic dispersion with the lattice boltzmann method, *Physical Review A* **45**, 5771 (1992).

[6] V. Turau, Fixed-radius near neighbors search, *Information Processing Letters* **39**, 201 (1991).

[7] L. Verlet, Computer "Experiments" on Classical Fluids. I. Thermodynamical Properties of Lennard-Jones Molecules, *Physical Review* **159**, 98 (1967).

[8] R. A. Gingold and J. J. Monaghan, Smoothed particle hydrodynamics: theory and application to non-spherical stars, *Monthly Notices of the Royal Astronomical Society* **181**, 375 (1977), <https://academic.oup.com/mnras/article-pdf/181/3/375/3104055/mnras181-0375.pdf>.

[9] V. Springel, N. Yoshida, and S. D. White, Gadget: a code for collisionless and gasdynamical cosmological simulations, *New Astronomy* **6**, 79 (2001).

[10] M. J. Abraham, T. Murtola, R. Schulz, S. Páll, J. C. Smith, B. Hess, and E. Lindahl, Gromacs: High performance molecular simulations through multi-level parallelism from laptops to supercomputers, *SoftwareX* **1-2**, 19 (2015).

[11] G. Di Ilio, D. Chiappini, S. Ubertini, G. Bella, and S. Succi, Fluid flow around naca 0012 airfoil at low-reynolds numbers with hybrid lattice boltzmann method, *Computers & Fluids* **166**, 200 (2018).

[12] Z. Yao, J.-S. Wang, G.-R. Liu, and M. Cheng, Improved neighbor list algorithm in molecular simulations using cell decomposition and data sorting method, *Computer Physics Communications* **161**, 27 (2004).

[13] J. Barnes and P. Hut, A hierarchical $O(N \log N)$ force-calculation algorithm, *Nature* **10.1038/324446a0** (1986).

[14] X. Chen and S. Güttel, *Fast and exact fixed-radius neighbor search based on sorting* (2024).

[15] L. Wang, Y. Wu, Y. Deng, B. Kim, L. Pierce, G. Krilov, D. Lupyán, S. Robinson, M. K. Dahlgren, J. Greenwood, D. L. Romero, C. Masse, J. L. Knight, T. Steinbrecher, T. Beuming, W. Damm, E. Harder, W. Sherman, M. Brewer, R. Wester, M. Murcko, L. Frye, R. Farid, T. Lin, D. L. Mobley, W. L. Jorgensen, B. J. Berne, R. A. Friesner, and R. Abel, Accurate and reliable prediction of relative ligand binding potency in prospective drug discovery by way of a modern free-energy calculation protocol and force field, *Journal of the American Chemical Society* **137**, 2695 (2015).

[16] Y. Shan, E. T. Kim, M. P. Eastwood, R. O. Dror, M. A. Seeliger, and D. E. Shaw, How does a drug molecule find its target binding site?, *Journal of the American Chemical Society* **133**, 9181 (2011).

[17] P. J. Bond and M. S. Sansom, Insertion and assembly of membrane proteins via simulation, *Journal of the American Chemical Society* **10.1021/ja0569104** (2006).

[18] C. Liu, L. Xue, and C. Song, Calcium binding and permeation in trpv channels: Insights from molecular dynamics simulations, *Journal of General Physiology* **155**, e202213261 (2023), epub 2023 Sep 20.

[19] H. Zhao, P. Duan, Z. Li, Q. Chen, T. Yue, L. Zhang, V. Ganeshan, and J. Liu, Unveiling the multiscale dynamics of polymer vitrimers via molecular dynamics simulations, *Macromolecules* **56**, 9336 (2023).

[20] M. P. Howard, J. A. Anderson, A. Nikoubashman, S. C. Glotzer, and A. Z. Panagiotopoulos, Efficient neighbor list calculation for molecular simulation of colloidal systems using graphics processing units, *Computer Physics Communications* **203**, 45 (2016).

[21] A. J. Proctor, T. J. Lipscomb, A. Zou, J. A. Anderson, and S. S. Cho, Performance Analyses of a Parallel Verlet Neighbor List Algorithm for GPU-Optimized MD Simulations, in *2012 ASE/IEEE International Conference on BioMedical Computing (BioMedCom)* (2012) pp. 14–19.

[22] F. Chiti and C. M. Dobson, Protein misfolding, amyloid formation, and human disease: A summary of progress over the last decade, *Annual Review of Biochemistry* **86**, 27 (2017).

[23] K. Lindorff-Larsen, S. Piana, R. O. Dror, and D. E. Shaw, How fast-folding proteins fold, *Science* **334**, 517 (2011).

[24] J. Abramson, J. Adler, J. Dunger, R. Evans, T. Green, A. Pritzel, O. Ronneberger, L. Willmore, A. J. Ballard, J. Bambrick, S. W. Bodenstein, D. A. Evans, C.-C. Hung, M. O'Neill, D. Reiman, K. Tunyasuvunakool, Z. Wu, A. Žemgulytė, E. Arvaniti, C. Beatrice, O. Bertolli, A. Bridgland, A. Cherepanov, M. Congreve, A. I. Cowen-Rivers, A. Cowie, M. Figurnov, F. B.

Fuchs, H. Gladman, R. Jain, Y. A. Khan, C. M. R. Low, K. Perlin, A. Potapenko, P. Savy, S. Singh, A. Stecula, A. Thillaisundaram, C. Tong, S. Yakneen, E. D. Zhong, M. Zielinski, A. Žídek, V. Bapst, P. Kohli, M. Jaderberg, D. Hassabis, and J. M. Jumper, Accurate structure prediction of biomolecular interactions with alphafold 3, *Nature* **630**, 493 (2024).

[25] K. Schütze, M. Heinzinger, M. Steinegger, and B. Rost, Nearest neighbor search on embeddings rapidly identifies distant protein relations, *Frontiers in Bioinformatics* **2**, 1033775 (2022).

[26] M. van Kempen, S. S. Kim, C. Tumescheit, M. Mirdita, J. Lee, C. L. M. Gilchrist, J. Söding, and M. Steinegger, Fast and accurate protein structure search with foldseek, *Nature Biotechnology* **42**, 243 (2024).

[27] P. Goloubinoff, M. Sulpizi, A. Cappellaro, J. Dutheil, H. A. Nguyen, and P. De Los Rios, Chaperones convert the energy from atp into the nonequilibrium stabilization of native proteins, *Nature Chemical Biology* **14**, 388 (2018).

[28] S. Assenza, A. S. Sassi, R. Kellner, P. De Los Rios, and A. Barducci, Efficient conversion of chemical energy into mechanical work by hsp70 chaperones, *Physical Review X* **9**, 041033 (2019).

[29] P. De Los Rios and A. Barducci, Non-equilibrium protein folding and activation by atp-driven chaperones, *Nature Reviews Molecular Cell Biology* **15**, 611 (2014).

[30] E. M. Sontag, R. S. Samant, and J. Frydman, Mechanisms and functions of spatial protein quality control, *Annual Review of Biochemistry* **86**, 97 (2017).

[31] C. L. Klaips, G. G. Jayaraj, and F. U. Hartl, Pathways of cellular proteostasis in aging and disease, *Journal of Cell Biology* **217**, 51 (2018).

[32] A. C. Crespo, J. M. Dominguez, A. Barreiro, M. Gómez-Gesteira, and B. D. Rogers, Gpus, a new tool of acceleration in cfd: Efficiency and reliability on smoothed particle hydrodynamics methods, *PLOS ONE* **6**, 1 (2011).

[33] V. Springel, The cosmological simulation code gadget-2, *Monthly notices of the royal astronomical society* **364**, 1105 (2005).

[34] Q. Zhu, L. Hernquist, and Y. Li, Numerical convergence in smoothed particle hydrodynamics, *The Astrophysical Journal* **800**, 6 (2015).

[35] T. L. Cassell, T. Deakin, A. Alpay, V. Heuveline, and G. B. Gadeschi, Efficient tree-based parallel algorithms for n-body simulations using c++ standard parallelism, in *SC24-W: Workshops of the International Conference for High Performance Computing, Networking, Storage and Analysis* (2024) pp. 708–717.

[36] supercomputer fugaku - fujitsu.

[37] T. Papatheodore, Summit architecture overview.

[38] J. I. Read and T. Hayfield, Sphs: smoothed particle hydrodynamics with a higher order dissipation switch, *Monthly Notices of the Royal Astronomical Society* **422**, 3037 (2012), <https://academic.oup.com/mnras/article-pdf/422/4/3037/18598311/mnras0422-3037.pdf>.

[39] M. Castelli, F. Marchetti, S. Osuna, A. S. F. Oliveira, A. J. Mulholland, S. A. Serapian, and G. Colombo, Decoding Allostery in Membrane-Bound K-Ras4B Using Complementary In Silico Approaches Based on Unbiased Molecular Dynamics Simulations, *Journal of the American Chemical Society* **146**, 901 (2024), publisher: American Chemical Society.

[40] D. Frenkel and B. Smit, *Understanding Molecular Simulation: From Algorithms to Applications*, 2nd ed. (Academic Press, 2002) Chap. 3.

[41] J. N. F. Alves, L. M. S. Russo, and A. Francisco, Cache-oblivious hilbert curve-based blocking scheme for matrix transposition, *ACM Transactions on Mathematical Software* **48**, 1 (2022).

[42] E. F. Combarro, I. F. Rúa, F. Orts, G. Ortega, A. M. Puertas, and E. M. Garzón, Quantum algorithms to compute the neighbour list of N-body simulations, *Quantum Information Processing* **23**, 61 (2024).

[43] M. Nielsen and I. Chuang, *Quantum Computation and Quantum Information: 10th Anniversary Edition* (Cambridge University Press, 2010).

[44] Y. Cao, J. Romero, J. P. Olson, M. Degroote, P. D. Johnson, M. Kieferová, I. D. Kivlichan, T. Menke, B. Peropadre, N. P. D. Sawaya, S. Sim, L. Veis, and A. Aspuru-Guzik, Quantum chemistry in the age of quantum computing, *Chemical Reviews* **119**, 10856 (2019).

[45] Y. Alexeev, M. Amsler, M. A. Barroca, S. Bassini, T. Battelle, D. Camps, D. Casanova, Y. J. Choi, F. T. Chong, C. Chung, C. Codella, A. D. Córcoles, J. Cruise, A. Di Meglio, I. Duran, T. Eckl, S. Economou, S. Eidenbenz, B. Elmegreen, C. Fare, I. Faro, C. S. Fernández, R. N. B. Ferreira, K. Fuji, B. Fuller, L. Gagliardi, G. Galli, J. R. Glick, I. Gobbi, P. Gokhale, S. de la Puente Gonzalez, J. Greiner, B. Gropp, M. Grossi, E. Gull, B. Healy, M. R. Hermes, B. Huang, T. S. Humble, N. Ito, A. F. Izmaylov, A. Javadi-Abhari, D. Jennewein, S. Jha, L. Jiang, B. Jones, W. A. de Jong, P. Jurcevic, W. Kirby, S. Kister, M. Kitagawa, J. Klassen, K. Klymko, K. Koh, M. Kondo, D. M. Kürkçüoğlu, K. Kurowski, T. Laino, R. Landfield, M. Leininger, V. Leyton-Ortega, A. Li, M. Lin, J. Liu, N. Lorente, A. Luckow, S. Martiel, F. Martin-Fernandez, M. Martonosi, C. Marvinney, A. C. Medina, D. Merten, A. Mezzacapo, K. Michielsen, A. Mitra, T. Mittal, K. Moon, J. Moore, S. Mostame, M. Motta, Y.-H. Na, Y. Nam, P. Narang, Y.-y. Ohnishi, D. Ottaviani, M. Otten, S. Pakin, V. R. Pascuzzi, E. Pednault, T. Piontek, J. Pitera, P. Rall, G. S. Ravi, N. Robertson, M. A. C. Rossi, P. Rydlichowski, H. Ryu, G. Samsonidze, M. Sato, N. Saurabh, V. Sharma, K. Sharma, S. Shin, G. Slessman, M. Steiner, I. Sittikov, I.-S. Suh, E. D. Switzer, W. Tang, J. Thompson, S. Todo, M. C. Tran, D. Trenev, C. Trott, H.-H. Tseng, N. M. Tubman, E. Tureci, D. G. Valinas, S. Vallecorsa, C. Wever, K. Wojciechowski, X. Wu, S. Yoo, N. Yoshioka, V. W.-z. Yu, S. Yunoki, S. Zhuk, and D. Zubarev, Quantum-centric supercomputing for materials science: A perspective on challenges and future directions, *Future Generation Computer Systems* **160**, 666 (2024).

[46] L. Cappelli, F. Tacchino, G. Murante, S. Borgani, and I. Tavernelli, From vlasov-poisson to schrödinger-poisson: Dark matter simulation with a quantum variational time evolution algorithm, *Phys. Rev. Res.* **6**, 013282 (2024).

[47] S. Succi, W. Itani, K. Sreenivasan, and R. Steijl, Quantum computing for fluids: Where do we stand?, *Europhysics Letters* **144**, 10001 (2023).

[48] L. K. Grover, A fast quantum mechanical algorithm for database search, in *Proceedings of the Twenty-Eighth Annual ACM Symposium on Theory of Computing*, STOC '96 (Association for Computing Machinery, New York, NY, USA, 1996) p. 212–219.

[49] L. K. Grover, Fixed-Point Quantum Search, *Physical Re-*

view Letters **95**, 150501 (2005).

[50] A. Mizel, Critically Damped Quantum Search, *Physical Review Letters* **102**, 150501 (2009).

[51] T. J. Yoder, G. H. Low, and I. L. Chuang, Fixed-Point Quantum Search with an Optimal Number of Queries, *Phys. Rev. Lett.* **113**, 210501 (2014).

[52] D. W. Berry, A. M. Childs, R. Cleve, R. Kothari, and R. D. Somma, Exponential improvement in precision for simulating sparse hamiltonians, *Forum of Mathematics, Sigma* **5**, 10.1017/fms.2017.2 (2017).

[53] B. Yan, S. Wei, H. Jiang, H. Wang, Q. Duan, Z. Ma, and G.-L. Long, Fixed-point oblivious quantum amplitude-amplification algorithm, *Scientific Reports* **12**, 14339 (2022), publisher: Nature Publishing Group.

[54] A. A. Zecchi, C. Sanavio, S. Perotto, and S. Succi, *Improved amplitude amplification strategies for the quantum simulation of classical transport problems* (2025).

[55] A. Gilyén, Y. Su, G. H. Low, and N. Wiebe, Quantum singular value transformation and beyond: exponential improvements for quantum matrix arithmetics, in *Proceedings of the 51st Annual ACM SIGACT Symposium on Theory of Computing* (ACM, Phoenix AZ USA, 2019) pp. 193–204.

[56] J. M. Martyn, Z. M. Rossi, A. K. Tan, and I. L. Chuang, Grand Unification of Quantum Algorithms, *PRX Quantum* **2**, 040203 (2021).

[57] D. Cesarini, F. Pitari, F. Barbari, F. Ficarelli, P. Lanucara, G. Cavallaro, E. Casarotti, I. Piljic', A. Beggs, O. Marsden, I. Hadade, L. Tornatore, V. Flouris, F. Nikolaidis, A. Bilas, E. Raffin, A. Morvan, O. Meca, R. Lubomir, T. Lohier, V. Brenner, L. Genovese, and M. Delorme, *EUPEX deliverable D3.2 Applications optimised for SVE and HBM*, Tech. Rep. (EuropeanUnion, 2023).

[58] S. Habib, V. Morozov, N. Frontiere, H. Finkel, A. Pope, K. Heitmann, K. Kumaran, V. Vishwanath, T. Peterka, J. Insley, D. Daniel, P. Fasel, and Z. Lukić, HACC: Extreme scaling and performance across diverse architectures, *Commun. ACM* **60**, 97 (2017).

[59] G. Brassard, P. Høyer, and A. Tapp, Quantum counting, in *Automata, Languages and Programming: 25th International Colloquium, ICALP'98 Aalborg, Denmark, July 13–17, 1998 Proceedings* 25 (Springer, 1998) pp. 820–831.

[60] S. Lee and S. Y. Nam, Finding all solutions with grover's algorithm by integrating estimation and discovery, *Electronics* **13**, 10.3390/electronics13234830 (2024).

[61] E. Malvetti, R. Iten, and R. Colbeck, Quantum Circuits for Sparse Isometries, *Quantum* **5**, 412 (2021), arXiv:2006.00016 [quant-ph].

[62] F. Mozafari, H. Riener, M. Soeken, and G. De Micheli, Efficient Boolean Methods for Preparing Uniform Quantum States, *IEEE Transactions on Quantum Engineering* **2**, 1 (2021).

[63] X.-M. Zhang, M.-H. Yung, and X. Yuan, Low-depth quantum state preparation, *Physical Review Research* **3**, 043200 (2021), publisher: American Physical Society.

[64] X.-M. Zhang, T. Li, and X. Yuan, Quantum State Preparation with Optimal Circuit Depth: Implementations and Applications, *Physical Review Letters* **129**, 230504 (2022), publisher: American Physical Society.

[65] X.-M. Zhang and X. Yuan, Circuit complexity of quantum access models for encoding classical data, *npj Quantum Information* **10**, 1 (2024), publisher: Nature Publishing Group.

[66] D. Camps, L. Lin, R. Van Beeumen, and C. Yang, *Explicit quantum circuits for block encodings of certain sparse matrices* (2024).

[67] C. Sanavio, W. A. Simon, A. Ralli, P. Love, and S. Succi, Carleman-lattice-Boltzmann quantum circuit with matrix access oracles, *Physics of Fluids* **37**, 037123 (2025).

[68] T. G. Draper, S. A. Kutin, E. M. Rains, and K. M. Svore, A logarithmic-depth quantum carry-lookahead adder, *Quantum Info. Comput.* **6**, 351–369 (2006).

[69] S. A. Cuccaro, T. G. Draper, S. A. Kutin, and D. P. Moulton, *A new quantum ripple-carry addition circuit* (2004).

[70] E. Thula, Quantum incrementer, <https://egrettathula.wordpress.com/2024/07/28/quantum-incrementer/>, july 28 2024.

[71] V. Shende, S. Bullock, and I. Markov, Synthesis of quantum-logic circuits, *IEEE Transactions on Computer-Aided Design of Integrated Circuits and Systems* **25**, 1000–1010 (2006).

[72] R. Vale, T. M. D. Azevedo, I. C. S. Araújo, I. F. Araújo, and A. J. da Silva, Circuit Decomposition of Multicon-trolled Special Unitary Single-Qubit Gates, *IEEE Transactions on Computer-Aided Design of Integrated Circuits and Systems* **43**, 802 (2024), conference Name: IEEE Transactions on Computer-Aided Design of Integrated Circuits and Systems.

[73] B. Zindorf and S. Bose, *Efficient Implementation of Multi-Controlled Quantum Gates* (2025), arXiv:2404.02279 [quant-ph].

[74] C. Figgatt, D. Maslov, K. A. Landsman, N. M. Linke, S. Debnath, and C. Monroe, Complete 3-Qubit Grover search on a programmable quantum computer, *Nature Communications* **8**, 1918 (2017).

[75] K. Zhang, K. Yu, and V. Korepin, Quantum search on noisy intermediate-scale quantum devices, *Europhysics Letters* **140**, 18002 (2022).

[76] J. Leng, F. Yang, and X.-B. Wang, Noise-tolerant Grover's algorithm via success-probability prediction, *Phys. Rev. Res.* **7**, L012017 (2025).

[77] S. Jaques and A. G. Rattew, Qram: A survey and critique, *Quantum* **9**, 1922 (2025).